

Rydberg Atomic Quantum Receivers for Wireless Communications: Two-Color vs. Three-Color Excitation

Jian Xiao, Tierui Gong, Ji Wang, Erry Gunawan, and Chau Yuen, Fellow, IEEE

Abstract—An efficient three-color (3C) laser excitation-based Rydberg atomic quantum receiver (RAQR) architecture is investigated for wireless communications, utilizing a five-level (5L) electronic transition mechanism. Specifically, the conventional two-color (2C) RAQR with the four-level (4L) excitation faces three fundamental obstacles: 1) high cost and engineering challenges due to the reliance on unstable short-wavelength lasers; 2) a fundamental sensitivity limit in thermal atoms caused by residual Doppler broadening; and 3) the inability to detect low-frequency bands due to the energy-level constraint of two-photon resonance. To address these challenges, this paper analyzes a 3C5L-RAQR architecture with all-red/infrared lasers, which not only solves the engineering cost issues but also enables effective Doppler cancellation and low-frequency detection by exhibiting the three-photon resonance. Bridging atomic physics and communication theory, an end-to-end equivalent baseband signal model is derived. Furthermore, the performance of different RAQR architectures is evaluated in terms of sensitivity, achievable capacity and spectrum access range. Moreover, we provide an exact numerical solution for practical RAQRs by employing the Liouvillian superoperator formalism. Numerical results demonstrate that the exhibited 3C5L-RAQR achieves superior sensitivity compared to the conventional 2C4L-RAQR and the classical radio-frequency receiver based on the conductor antenna. Finally, the inherent sensitivity-capacity trade-off is revealed, showing that the 3C5L-RAQR is more suitable for deployment in power-limited communication scenarios demanding broad spectrum access.

Index Terms—Rydberg atomic quantum receivers, thermal atoms, Doppler broadening, performance analysis.

I. Introduction

RYDBERG atomic sensors have been extensively investigated for decades as highly sensitive detection tools, leveraging the giant electric dipole moments of Rydberg atoms [1]. More recently, a significant research trend has emerged that seeks to extend the capabilities of these atomic systems from pure sensing to the domain of wireless communications [2], [3]. While the Rydberg atom configuration exhibits enhanced sensitivity via coherent control, these gains are inevitably accompanied by an inherent trade-off that follows the no free lunch theorem for any scientific research [4]. Specifically, the heightened complexity of the atom resonance alignment by expensive and large laser equipment and the narrower spectral

windows suggest that the quantum advantage may be constrained to specific operational regimes [5].

A. Background of Rydberg Atomic Quantum Receivers

Historically, the development of applying the Rydberg atom to the radio frequency (RF) domain progressed through two primary stages. The first phase, primarily driven by the physics and quantum optics communities, focused on fundamental experimental verification for the RF signal detection with Rydberg atoms [6]. During this period, significant experimental progress has been made in demonstrating the capabilities of RAQRs, including digital communications [2] using electromagnetically induced transparency (EIT) effect, signal reception under various modulations [7], and multi-band detection by utilizing different Rydberg transitions [8].

The second stage, which rose to prominence from 2024 to the present, marks a shift toward a telecommunications-oriented perspective. Researchers started leveraging Rydberg physical models for various communication scenarios, e.g., multiple input multiple output (MIMO) communications [9], [10], and wireless sensing [11]–[13]. In this stage, this receiver architecture is termed the Rydberg atomic quantum receiver (RAQR) [11] or Rydberg atomic receiver (RARE) [13]. Unlike the experimental nature of the first phase, this recent wave of research is predominantly theoretical, relying on simulations to verify concepts. As such, these system-level applications are still in their infancy and require further validation.

B. Motivations for New RAQR Architectures

Currently, the research landscape of RAQR-aided wireless systems is predominantly focused on the conventional two-color (2C) laser architecture [9]–[13], employing a ladder-type excitation scheme to realize the four-level (4L) electronic transition of Rydberg atoms. The 2C4L-RAQR utilizes a probe laser and a coupling laser to drive the atoms into a coherent dark state via two-photon resonance. However, despite the established efficacy of the conventional 2C4L-RAQR, it is constrained by three fundamental limitations:

- 1) **The Engineering and Cost Problem:** The reliance on a high-power short-wavelength laser, e.g., the wavelength of coupling laser $\lambda_c \approx 480 - 510$ nm [14], is a major engineering barrier. The blue laser is notoriously expensive, physically bulky, and high-power [15], which makes the standard 2C4L-RAQR

Jian Xiao and Ji Wang are with the Department of Electronics and Information Engineering, College of Physical Science and Technology, Central China Normal University, Wuhan 430079, China. (e-mail: jianx@mails.ccnu.edu.cn; jiwang@ccnu.edu.cn).

Tierui Gong, Erry Gunawan and Chau Yuen are with the School of Electrical and Electronics Engineering, Nanyang Technological University, Singapore 639798. (e-mail: tierui.gong@ntu.edu.sg; egunawan@ntu.edu.sg; chau.yuen@ntu.edu.sg).

impractical for low-cost, compact or field-deployable units.

- 2) The Fundamental Sensitivity Limit: The sensitivity of RAQR is inversely proportional to the linewidth of EIT. In a room-temperature thermal vapor cell, the 4L transition scheme with 2C lasers suffers from a large wavelength mismatch between the infrared probe and the blue/green coupling lasers. The residual Doppler broadening creates a fundamental floor for the EIT linewidth and masks the atomic response to weak signals, creating a bottleneck for ultimate sensitivity [16].
- 3) The Frequency Access Limit: In the typical 2C4L excitation scheme, atoms are driven to a Rydberg D -state with orbital angular momentum $l = 2$ [11, Table 1]. Resonant detection from these D -states is physically constrained by the large energy gaps to the adjacent allowed states, restricting the detectable frequencies to the high-GHz or THz range [17]¹. The high-sensitivity detection relying on natural resonance of Rydberg atoms is fundamentally inaccessible to the 2C4L-RAQR in the low-frequency band, e.g., very-high frequency (VHF) to ultra-high-frequency (UHF) bands.

To address above limitations, recent physics experiments explored three-color (3C) RAQR architecture, i.e., utilizing three lasers with distinct wavelengths to construct the five-level (5L) excitation of Rydberg atoms. The authors of [14] demonstrated an all-infrared 3C scheme to achieve EIT, proving the feasibility of low-cost diode lasers. Furthermore, the authors of [16] demonstrated that 3C5L electrometry yields a narrower linewidth and higher sensitivity compared to the 2C4L architecture due to superior Doppler cancellation. Moreover, in [22], the resonant detection of RF electric fields from VHF to UHF bands was implemented by using 3C5L-RAQR to construct the high orbital angular momentum Rydberg states.

While the theoretical physical foundations of 3C5L-RAQR have shown great potential as a new architecture, these existing works are predominantly focused on static field electrometry or spectroscopy. However, the communication-centric modeling and analysis for 3C5L-RAQR assisted wireless communications remain largely unexplored.

C. Contributions

Against the aforementioned background, in this paper, we investigate the 3C5L-RAQR architecture for wireless communications. Our main contributions are summarized as follows:

¹For detecting strategic low-frequency bands, the conventional transition scheme in the 2C4L-RAQR can use inefficient off-resonant mechanisms, e.g., alternating current (AC) Stark shift [18], [19], but inherently limits sensitivity. While direct current (DC) Stark tuning can be used to force a resonance [20], [21], this alternative method introduces significant line-broadening noise and technical complexity from the strong external DC field.

- We establish the physical model for the 3C5L excitation scheme with low-cost all-red/infrared lasers and identify the residual Doppler broadening as the fundamental sensitivity bottleneck in thermal vapor cells for practical RAQRs. Furthermore, we derive an end-to-end equivalent baseband signal model that maps the physical atom interaction to standard communication model.
- We formulate the scaling laws of SNR for 2C4L- and 3C5L-RAQRs in different quantum noise regimes under the weak probe field. Then, we reveal that the achievable channel capacity of the RAQR is restricted by the limited instantaneous bandwidth that is related to the transient relaxation time of the Rydberg atoms. We also prove that the 3C5L-RAQR serves as a unified platform capable of accessing strategic UHF/VHF bands via high-angular-momentum transitions.
- We propose an efficient numerical modeling of open quantum dynamics for practical RAQRs, which surpasses the classic assumption of the weak probe field to achieve the superior receiver performance. By employing the Liouvillian superoperator formalism and the eigendecomposition of the non-Hermitian Liouvillian matrix, we provide the exact numerical solution for atomic coherence and baseband bandwidth of the 3C5L-RAQR under practical thermal atom environments.
- We demonstrate through numerical results that the exhibited 3C5L-RAQR with thermal robustness outperforms the 2C4L-RAQR and the classic RF receiver in terms of signal-to-noise ratio (SNR) gain and block error rate (BLER) performance. Due to limited instantaneous bandwidth, the RAQR is more suitable for deployment in power-limited and spectrum-agile communication scenarios, while the classic RF receiver retains an advantage in high-speed communications.

Notations: $|i\rangle$ denotes the i -th atomic state and $\langle i|$ denotes its corresponding bra vector. $\langle i|\hat{\rho}|j\rangle$ represents the matrix element of density operator $\hat{\rho}$ between state $|i\rangle$ and $|j\rangle$. The dot notation in $\dot{\rho}$ represents the first time derivative $d\rho/dt$. $|nL_J\rangle$ denotes atomic states, where n is the principal quantum number, L is the orbital angular momentum quantum number, e.g., S for $l = 0$, P for $l = 1$, D for $l = 2$, F for $l = 3$, and J is the total angular momentum quantum number. i denotes the imaginary unit. Operators $\Re(\cdot)$, $\Im(\cdot)$ and $\arg(\cdot)$ denote the real, imaginary and phase components of the complex-value elements. Operator $(\cdot)^*$ denotes the conjugate of complex-value elements. Operators $(\cdot)^{-1}$ and $\det(\cdot)$ denote the inverse and determinant of a matrix, respectively. Symbols q_0 and a_0 denote elementary charge and Bohr radius, respectively.

II. Physical Architectures and Signal Models

In this section, we first establish the physical models for different RAQR architectures. Then, we derive the

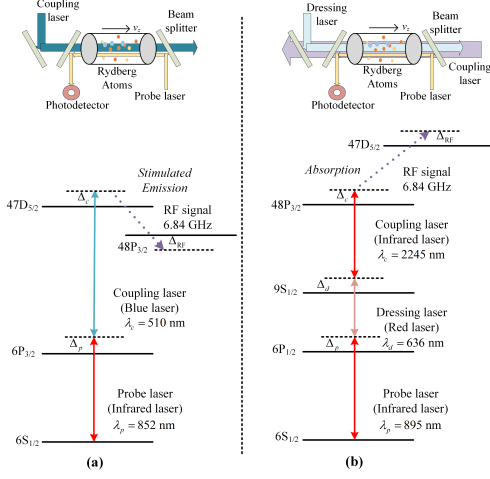


Fig. 1. Atomic energy level schemes for Cs atoms [16]. (a) The conventional 2C4L-RAQR with electronic transition path $6S \rightarrow 6P \rightarrow nD$, which is driven by an infrared probe laser with wavelength $\lambda_p = 852$ nm and a high-power green coupling laser with wavelength $\lambda_c = 510$ nm. (b) The exhibited 3C5L-RAQR with transition path $6S \rightarrow 6P \rightarrow 9S \rightarrow n'P$, which uses low-cost diode lasers, i.e., an infrared probe laser with wavelength $\lambda_p = 895$ nm, a red dressing laser with wavelength $\lambda_d = 636$ nm, and an infrared coupling laser with wavelength $\lambda_c = 2245$ nm. Note that considering the same incident RF signal, the 2C4L-RAQR carries out the downward electronic transitions based on the stimulated emission mechanism [23], i.e., $|47D_{5/2}\rangle \rightarrow |48P_{3/2}\rangle$, while the 3C5L-RAQR achieves the upward transitions via the energy absorption, i.e., $|48P_{3/2}\rangle \rightarrow |47D_{5/2}\rangle$.

communication baseband signal model of the exhibited 3C5L-RAQR.

A. Conventional 2C4L-RAQR Architectures

In this section, we review the physical architectures of the conventional 2C4L-RAQR to provide a comparative baseline.

1) System Architecture: As shown in Fig. 1(a), the standard 2C4L-RAQR operates on a 4L electronic transition scheme. A common example in Cesium (Cs) atoms is $|1\rangle = |6S_{1/2}\rangle \rightarrow |2\rangle = |6P_{3/2}\rangle \rightarrow |3\rangle = |nD_J\rangle$. The microwave signal couples $|3\rangle$ to an adjacent state $|4\rangle$. This excitation pathway requires an infrared probe laser with wavelength λ_p and a green coupling laser with wavelength λ_c . This reliance on a high-power green laser $\lambda_c = 510$ nm [15], constitutes the major engineering problem, which makes the standard 2C4L-RAQR impractical for low-cost, compact, or field-deployable units.

2) Physical Modeling: The coherent dynamics of the 2C4L electronic transition are driven by a probe laser, a coupling laser, and a RF signal field. The evolution is governed by the Lindblad master equation [24], [25], which is given by

$$\frac{d\hat{\rho}}{dt} = -\frac{i}{\hbar}[\hat{H}_{4L}, \hat{\rho}] + \mathcal{L}(\hat{\rho}), \quad (1)$$

where $\hat{\rho}$ is the atomic density matrix and \hbar denotes the reduced Planck constant. \hat{H}_{4L} denotes the Hamiltonian for the 2C4L-RAQR system. $\mathcal{L}(\hat{\rho})$ describes all spontaneous decay and dephasing processes.

To find the steady-state coherence $\rho_{21} = \langle 2|\hat{\rho}|1\rangle$, we solve $\hat{\rho} = \frac{d\hat{\rho}}{dt} = 0$. By utilizing the specific assumptions

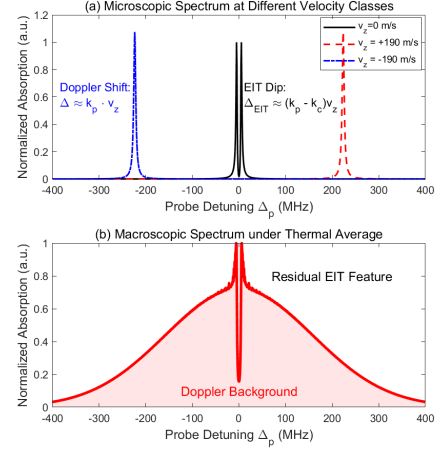


Fig. 2. EIT absorption spectrum $\Im(\hat{\rho}_{21}^{4L})$ vs. probe detuning Δ_p .

and approximations, different analytical solutions of ρ_{21} have been derived [25]–[27]. Considering the classic weak-probe approximation², the steady-state coherence ρ_{21}^{4L} for 2C4L-RAQR can be expressed as [27]

$$\rho_{21}^{4L} = \frac{i\Omega_p^{4L}/2}{(i\Delta_2^{4L} - \Gamma_{21}) + \frac{|\Omega_c^{4L}|^2/4}{(i\Delta_3^{4L} - \Gamma_{31}) + \frac{|\Omega_{RF}|^2/4}{i\Delta_4^{4L} - \Gamma_{41}}}}, \quad (2)$$

where Ω_p^{4L} , Ω_c^{4L} , and Ω_{RF} are the Rabi frequencies of the probe, coupling, and RF fields for the 2C4L-RAQR, respectively. $\Delta_2^{4L} = \Delta_p^{4L}$, $\Delta_3^{4L} = \Delta_p^{4L} + \Delta_c^{4L}$, and $\Delta_4 = \Delta_3^{4L} + \Delta_{RF}$. Here, Δ_p^{4L} , Δ_c^{4L} , and Δ_{RF} are the corresponding frequency detunings from their atomic resonances. Γ_{n1} , $n \in \{2, \dots, 5\}$ are the coherence decay rates between states $|n\rangle$ and $|1\rangle$. Each Γ_{n1} is the sum of all processes that destroy the phase coherence between the two states. If collisional dephasing is negligible, we have $\Gamma_{n1} = \frac{1}{2}(\Gamma_n + \Gamma_1)$ [27], where Γ_n and Γ_1 are the natural decay rates of the excited state $|n\rangle$ and the ground state, respectively. Γ_1 is usually set to 0 as the ground state is stable, so the relation simplifies to $\Gamma_{n1} = \frac{\Gamma_n}{2}$. Note that in the EIT linewidth modeling of Section III-A, the detailed components for total dephasing rate are investigated.

The optical response of the receiver is determined by the bulk atomic susceptibility χ , which can be expressed as [25]

$$\chi = \frac{N_a |\mu_{12}|^2}{\epsilon_0 \hbar \Omega_p} \rho_{21}, \quad (3)$$

where N_a is the effective density of atoms populating the ground state $|1\rangle$, μ_{12} is the dipole moment of the $|1\rangle \rightarrow |2\rangle$ transition, and ϵ_0 is the vacuum permittivity.

3) Physical Limitation: The EIT mechanism in the 2C4L-RAQR relies on precise ladder-type transition resonance between the probe and coupling laser fields, i.e.,

²From the perspective of sensitivity optimization, the classic weak-probe approximation in the RAQR is suboptimal [28], particularly for the practical thermal atoms with severe Doppler broadening. In this section, to gain theoretical and explainable insights into the fundamental sensitivity bottlenecks for the subsequent performance analysis, we first present the atomic coherence under the ideal weak-probe approximation, while we provide the exact numerical modeling of ρ_{21} for general probe fields in Section IV.

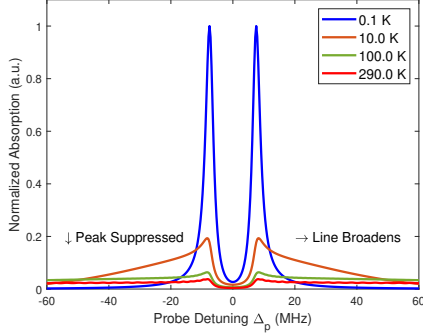


Fig. 3. EIT absorption spectrum $\Im(\rho_{21}^{4L})$ vs. probe detuning Δ_p for different thermal-atom temperature T_{atom} of vapor cell.

$\Delta_p^{4L} + \Delta_c^{4L} = 0$. In a thermal vapor cell, an atom moving with velocity \vec{v} perceives the laser frequencies shifted by the Doppler effect $\Delta_j(\vec{v}) = \Delta_j - \vec{k}_j \cdot \vec{v}$, where \vec{k}_j is the wavevector of the j -th laser field. To minimize the Doppler mismatch, the probe and coupling beams are configured to be counter-propagating. We define the propagation direction of the probe beam as the positive z -axis and v_z is the longitudinal velocity component of thermal atom motion, such that $\vec{k}_p = k_p \hat{z}$ and $\vec{k}_c = -k_c \hat{z}$, where $k_j = 2\pi/\lambda_j$ denotes the wavenumber. Consequently, for an atom moving with a velocity vector $\vec{v} \approx v_z \hat{z}$ along the optical axis under vapor cell temperature T_{atom} , the effective detuning in the 2C4L-RAQR is given by [27], [29]

$$\begin{aligned} \Delta_{\text{EIT}}^{4L} &= (\Delta_p^{4L} - \vec{k}_p \cdot \vec{v}) + (\Delta_c^{4L} - \vec{k}_c \cdot \vec{v}) \\ &= (\Delta_p^{4L} + \Delta_c^{4L}) + (k_c - k_p)v_z. \end{aligned} \quad (4)$$

Fig. 2 illustrates the microscopic origin of the sensitivity limit in thermal vapor cells. (a) Individual velocity classes of atoms experience different Doppler shifts, effectively smearing the resonance across the frequency domain. (b) The macroscopic response under Doppler-averaging, obtained by integrating over the Maxwell-Boltzmann distribution [16], [24], [25], [28], reveals that the sharp EIT feature is severely broadened into a wide Doppler background. Fig. 3 further presents the impact of thermal field on the EIT linewidth. As the temperature T_{atom} of the vapor cell increases from 0.1 K (quasi-cold state) to 290 K (room-temperature state), the thermal velocity of the atoms increases, leading to severe Doppler broadening, where the EIT window widens significantly.

Due to the large wavelength difference between the probe and coupling lasers, the wavevectors do not match. Even with counter-propagating beams, the cancellation is imperfect, i.e., $|k_p - k_c| \gg 0$, leading to a partial cancellation of the Doppler broadening effect. According to [16], the uncanceled residual Doppler linewidth in the 2C4L-RAQR can be expressed as

$$\Gamma_{\text{Res}}^{4L} = \frac{\Gamma_2}{|k_p|} |k_p - k_c|, \quad (5)$$

where Γ_2 is the decay rate of the first excited state $|2\rangle$. This calculation yields a large residual linewidth Γ_{Res}^{4L} on the order of several MHz.

The fundamental sensitivity of the RAQR is limited by the linewidth of the EIT linewidth Γ_{EIT} , where a narrower

Γ_{EIT} results in a higher sensitivity. Since the homogeneous broadening terms, e.g., natural linewidth, transit time, are typically in the order of kHz, the total EIT linewidth Γ_{EIT}^{4L} for the 4L system is dominated by this residual Doppler mismatch Γ_{Res}^{4L} [16]. This broad MHz-scale linewidth flattens the dispersion curve, masking the atomic response to weak RF signals and creating a fundamental sensitivity bottleneck. Moreover, the $S \rightarrow P \rightarrow D$ excitation pathway populates D -states, i.e., orbital angular momentum $l = 2$. Allowed RF transitions from D -states, e.g., $nD \rightarrow n'P$, have large energy gaps, corresponding to high frequencies, e.g., GHz/THz. However, the 2C4L-RAQR architecture is physically incapable of detecting strategic low-frequency UHF (300 MHz~3 GHz) or VHF (30 MHz~300 MHz) bands.

B. Exhibited 3C5L-RAQR for Doppler-Free Excitation

To overcome both the engineering and sensitivity limits inherent in the conventional 2C4L-RAQR configuration, we employ the Doppler-free 3C5L-RAQR excitation scheme recently demonstrated in physics experiments [16], [30], as shown in Fig. 1(b). In particular, we quantify the residual Doppler linewidths for both RAQR architectures and evaluate their macroscopic spectral responses, demonstrating the Doppler-free superiority in the 3C5L-RAQR.

1) System Architecture: The excitation path is $|1\rangle = |6S_{1/2}\rangle \xrightarrow{\Omega_p^{5L}} |2\rangle = |6P_{1/2}\rangle \xrightarrow{\Omega_d^{5L}} |3\rangle = |9S_{1/2}\rangle \xrightarrow{\Omega_c^{5L}} |4\rangle = |n'P_{J'}\rangle$, where Ω_p^{5L} , Ω_d^{5L} , and Ω_c^{5L} are the Rabi frequencies of the probe, dressing, and coupling fields for the 3C5L-RAQR, respectively. The three fields are red/infrared lasers, which excites state $|4\rangle$ via three stable and low-cost diode lasers.

2) Physical Modeling: The dynamics in 3C5L-RAQR are governed by the master equation using the 5L Hamiltonian:

$$\hat{H}_{5L} = \frac{\hbar}{2} \begin{pmatrix} 0 & \Omega_p^{5L} & 0 & 0 & 0 \\ (\Omega_p^{5L})^* & -2\Delta_2^{5L} & \Omega_d^{5L} & 0 & 0 \\ 0 & (\Omega_d^{5L})^* & -2\Delta_3^{5L} & \Omega_c^{5L} & 0 \\ 0 & 0 & (\Omega_c^{5L})^* & -2\Delta_4^{5L} & \Omega_{\text{RF}} \\ 0 & 0 & 0 & (\Omega_{\text{RF}})^* & -2\Delta_5^{5L} \end{pmatrix}, \quad (6)$$

where $\Delta_2^{5L} = \Delta_p^{5L}$, $\Delta_3^{5L} = \Delta_p^{5L} + \Delta_d^{5L}$, $\Delta_4^{5L} = \Delta_3^{5L} + \Delta_c^{5L}$, $\Delta_5^{5L} = \Delta_4^{5L} + \Delta_{\text{RF}}$. Here, Ω_d^{5L} and Δ_d^{5L} denote the newly introduced Rabi frequency and the corresponding frequency detuning of the dressing laser, respectively.

Lemma 1: Under the weak probe approximation [31], i.e., $\rho_{11}^{5L} \approx 1$ and $\rho_{ii \neq 1}^{5L} \approx 0$, the steady-state coherence ρ_{21}^{5L} for the 3C5L-RAQR can be expressed as

$$\rho_{21}^{5L} = \frac{i\Omega_p^{5L}/2}{(i\Delta_2 - \Gamma_{21}) + \frac{|\Omega_d^{5L}|^2/4}{(i\Delta_3 - \Gamma_{31}) + \frac{|\Omega_c^{5L}|^2/4}{(i\Delta_4 - \Gamma_{41}) + \frac{|\Omega_{\text{RF}}|^2/4}{i\Delta_5 - \Gamma_{51}}}}}. \quad (7)$$

Proof: Please refer to Appendix A for more details. ■

3) Physical Advantages: In 3C5L-RAQR system, the EIT condition depends on three-photon resonance, i.e., $\Delta_p^{5L} + \Delta_d^{5L} + \Delta_c^{5L} = 0$. We choose a counter-propagating geometry, e.g., \vec{k}_p and \vec{k}_c co-propagating, \vec{k}_d counter-

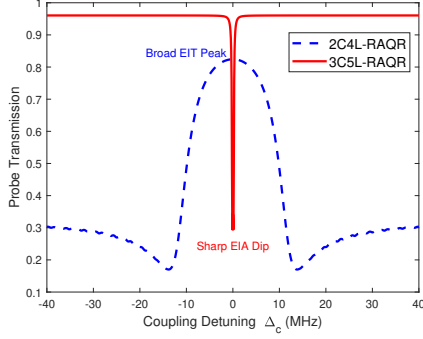


Fig. 4. Transmission spectrum vs. coupling detuning Δ_c under room temperature $T_{\text{atom}} = 290\text{K}$ of vapor cell.

propagating. The total velocity-dependent detuning becomes

$$\Delta_{\text{EIT}}^{5\text{L}} = (\Delta_{\text{p}}^{5\text{L}} + \Delta_{\text{c}}^{5\text{L}} + \Delta_{\text{d}}^{5\text{L}}) + (k_{\text{p}} - k_{\text{d}} + k_{\text{c}})v_z. \quad (8)$$

Unlike the previous 4L excitation scheme dominated by a $k_{\text{p}} - k_{\text{c}}$ mismatch, the entire sum nearly vanishes. The residual Doppler broadening is given by

$$\Gamma_{\text{Res}}^{5\text{L}} = \frac{\Gamma_2}{|k_{\text{p}}|} |k_{\text{p}} - k_{\text{d}} + k_{\text{c}}| \ll \Gamma_{\text{Res}}^{4\text{L}}. \quad (9)$$

Consequently, the EIT linewidth $\Gamma_{\text{EIT}}^{5\text{L}}$ for the 3C5L-RAQR is no longer limited by Doppler mismatch $\Gamma_{\text{Res}}^{5\text{L}}$ but rather by the much smaller homogeneous broadening terms. Fig. 4 presents a transmission spectrum of the steady-state probe transmission power, which is calculated by Eq. (13) in Section II-C. The 2C4L-RAQR exhibits a broad EIT window due to the uncanceled Doppler effects. Conversely, the 3C5L-RAQR maintains a sharp electromagnetic induced absorption (EIA) dip³. The narrower linewidth of the 5L signal implies a significantly larger gradient with respect to frequency changes, which directly translates to a higher optical response for a given RF field strength.

For the flexibility of spectrum access, while the 3C5L-RAQR uses a $P \rightarrow D$ transition for fairness with 2C4L-RAQR in Fig. 1, the $S \rightarrow P \rightarrow S \rightarrow P$ excitation path is also evolved into the $S \rightarrow P \rightarrow D \rightarrow F$ scheme [22]. In this case, the 3C5L-RAQR populates F-states, which unlocks access to high- l transitions, e.g., $|nF\rangle \rightarrow |nG\rangle$, $l = 3 \rightarrow l = 4$, preserving the advantage of UHF/VHF access.

C. Baseband Signal Model of 3C5L-RAQR

In this section, we incorporate the specific 3C5L excitation modeling to formulate the tailored equivalent baseband signal model for the 3C5L-RAQR, where the superheterodyne method is employed to detect the weak RF signal-induced atomic response [26], [32]. This approach alleviates the detector noise inherent in traditional RAQRs that rely on the phase-insensitive Autler-Townes splitting (ATS) effect [9], [33], [34].

³In practice, the presentation of EIT or EIA window in the 3C5L-RAQR depends on the relative intensity between the probe laser and the coupling laser [16, Fig.2]. Here, we consider a setup of weak probe field for deriving Eq. (7), and hence forming the EIA window.

1) Superheterodyne-Based Atomic Sensing: In a typical superheterodyne RAQR architecture, a weak incoming RF signal field U_x which carries the information at a carrier frequency f_c is mixed with a strong coherent LO field U_y at a nearby frequency f_l . This mixing process down-converts the signal to a low intermediate frequency (IF) $f_\delta = f_c - f_l$. The combined field $\Omega_{\text{RF}}(t)$ can be decomposed into a strong static field Ω_{LO} and a weak signal field $\Omega_{\text{sig}}(t)$ that oscillates at the IF, which is given by

$$\Omega_{\text{RF}}(t) = \Omega_{\text{LO}} + \Omega_{\text{sig}}(t) = \Omega_{\text{LO}} + \Omega_x \cos(2\pi f_\delta t + \theta_\delta), \quad (10)$$

where Ω_x is the Rabi frequency of the signal related to its electric field (E-field) U_x by $\Omega_x = \mu_{45} U_x / \hbar \ll |\Omega_{\text{LO}}|$ for the 5L $|4\rangle \rightarrow |5\rangle$ transition, and the IF phase is $\theta_\delta = \theta_x - \theta_y$, i.e., the signal phase θ_x relative to LO phase θ_y .

Suppose the input probe $P_0(t)$ is expressed as

$$P_0(t) = \sqrt{2\mathcal{P}_0} \cos(2\pi f_p t + \phi_0), \quad (11)$$

where \mathcal{P}_0 , f_p , and ϕ_0 are initial power, frequency, and phase of input probe, respectively.

The probe beam $P_0(t)$ propagates through the vapor cell with length d and is modulated by the susceptibility χ . Given the wavelength of the probe laser λ_p and the length of the vapor cell d , the output probe beam $P(\Omega_{\text{RF}}, t)$ in RAQRs is given by [25], [26]

$$P(\Omega_{\text{RF}}, t) = \sqrt{2\mathcal{P}_1(\Omega_{\text{RF}})} \cos(2\pi f_p t + \phi_p(\Omega_{\text{RF}})), \quad (12)$$

where the output power \mathcal{P}_1 and phase ϕ_p are given by

$$\mathcal{P}_1(\Omega_{\text{RF}}) = \mathcal{P}_0 e^{-\frac{2\pi d}{\lambda_p} \Im(\chi(\Omega_{\text{RF}}))}, \quad (13)$$

$$\phi_p(\Omega_{\text{RF}}) = \phi_0 + \frac{\pi d}{\lambda_p} \Re(\chi(\Omega_{\text{RF}})). \quad (14)$$

Since $\Omega_{\text{RF}}(t)$ is time-varying, both \mathcal{P}_1 and ϕ_p are modulated in time. We linearize them around the strong LO bias Ω_{LO} using a Taylor expansion, which can be expressed as

$$\chi(\Omega_{\text{RF}}) \approx \chi(\Omega_{\text{LO}}) + \Omega_{\text{sig}}(t)\chi'_s, \quad (15)$$

where $\chi'_s = \left. \frac{\partial \chi}{\partial \Omega_{\text{RF}}} \right|_{\Omega_{\text{LO}}}$ is the atomic transconductance. Substituting it into Eq. (14), we obtain the phase modulation as

$$\begin{aligned} \phi_p(\Omega_{\text{RF}}) &\approx \phi_0 + \frac{\pi d}{\lambda_p} \Re(\chi_0 + \Omega_{\text{sig}}(t)\chi'_s) \\ &= \left(\phi_0 + \frac{\pi d}{\lambda_p} \Re(\chi_0) \right) + \frac{\pi d}{\lambda_p} \Re(\Omega_{\text{sig}}(t)\chi'_s). \end{aligned} \quad (16)$$

Substituting it into Eq. (13) and using $e^x \approx 1 + x$ for the small signal term, we obtain the amplitude modulation as

$$\begin{aligned} \mathcal{P}_1(\Omega_{\text{RF}}) &\approx \mathcal{P}_0 e^{-\frac{2\pi d}{\lambda_p} \Im(\chi_0)} e^{-\frac{2\pi d}{\lambda_p} \Im(\Omega_{\text{sig}}(t)\chi'_s)} \\ &\approx \mathcal{P}_1(\Omega_{\text{LO}}) \left(1 - \frac{2\pi d}{\lambda_p} \Im(\Omega_{\text{sig}}(t)\chi'_s) \right). \end{aligned} \quad (17)$$

Hence, the weak RF signal $\Omega_{\text{sig}}(t)$ has successfully modulated both the amplitude and phase of the optical probe beam.

2) BCOD-Based Photoelectric Detection: To detect the strength of the optical probe beam modulated by the impinging RF field, we adopt the balanced coherent optical detection (BCOD) scheme [26]. BCOD utilizes a strong local optical beam, which helps to suppress the thermal noise generated by electronic components. Let the optical LO in BCOD be $P_l(t) = \sqrt{2\mathcal{P}_l} \cos(2\pi f_p t + \phi_l)$,

where \mathcal{P}_l and ϕ_l are the power and phase of optical LO, respectively. BCOD mixes the modulated probe beam $P(\Omega_{\text{RF}}, t)$ with the optical LO $P_l(t)$. The two beams are combined on a beam splitter, and the two outputs are sent to two photodiodes. The balanced detector subtracts the resulting photocurrents, which cancels out the large DC components and isolates the product of the two optical fields, forming the baseband photocurrent as [26]

$$I_B(t) = 2\alpha\sqrt{\mathcal{P}_l\mathcal{P}_1(\Omega_{\text{RF}})}\cos(\phi_l - \phi_p(\Omega_{\text{RF}})), \quad (18)$$

where α is the photodetector responsivity.

The photocurrent signal $I_B(t)$ is fed to a transimpedance amplifier (TIA) with load R and a low noise amplifier (LNA) with power gain G_{PD} , and hence the output voltage $V_B(t) = \sqrt{G_{\text{PD}}RI_B(t)}$. Substituting the photocurrent from Eq. (18) and assuming a unit value R of impedance load, we get

$$V_B(t) = \sqrt{G_{\text{PD}}}\left[2\alpha\sqrt{\mathcal{P}_l\mathcal{P}_1(\Omega_{\text{RF}})}\cos(\phi_l - \phi_p(\Omega_{\text{RF}}))\right]. \quad (19)$$

We define $P_{\text{mix}}(\Omega_{\text{RF}}) \triangleq \sqrt{\mathcal{P}_1(\Omega_{\text{RF}})}\cos(\phi_l - \phi_p(\Omega_{\text{RF}}))$ and linearize this measured term around Ω_{LO} as

$$P_{\text{mix}}(t) \approx P_{\text{mix}}(\Omega_{\text{LO}}) + \Omega_{\text{sig}}(t)\left.\frac{dP_{\text{mix}}}{d\Omega_{\text{RF}}}\right|_{\Omega_{\text{LO}}}. \quad (20)$$

The total voltage can be rewritten as $V_B(t) = V_{\text{DC}} + \tilde{V}(t)$, where $V_{\text{DC}} = 2\alpha\sqrt{G_{\text{PD}}\mathcal{P}_l\mathcal{P}_1(\Omega_{\text{LO}})}$ is the large DC offset, and $\tilde{V}(t) = 2\alpha\sqrt{G_{\text{PD}}\mathcal{P}_l}\Omega_{\text{sig}}(t)P'_{\text{mix}}(\Omega_{\text{LO}})$ is the desired AC signal at the IF that contains the impinging microwave signal.

Lemma 2: The desired AC component $\tilde{V}(t)$ at the IF f_δ in the 3C5L-RAQR is given by

$$\tilde{V}(t) = 2\alpha\sqrt{G_{\text{PD}}\mathcal{P}_l\mathcal{P}_1(\Omega_{\text{LO}})\kappa_1\sin(\varphi_1)}U_x\cos(2\pi f_\delta t + \theta_\delta), \quad (21)$$

where the field-to-optical gain κ_1 and the total atomic-optical phase shift φ_1 are given by

$$\kappa_1 \triangleq \frac{\pi d\mu_{45}}{\lambda_p \hbar} |\chi'_s|, \quad (22)$$

$$\varphi_1 = \phi_l - \phi_p(\Omega_{\text{LO}}) - \psi_p, \quad (23)$$

where $\psi_p = \arg(\chi'_s)$.

Proof: Please refer to Appendix B for more details. ■

3) Equivalent Baseband Signal Model: Next, we map the physical passband model in Eq. (21) to the complex baseband communication model. We define a complex baseband transfer function $\mathcal{H}_{\text{RAQR}}$ to link the received baseband signal $x_b(t)$ to the output baseband voltage $\tilde{V}_b(t)$ via the linear relation, i.e., $\tilde{V}_b(t) = \mathcal{H}_{\text{RAQR}}x_b(t)$. To find $\mathcal{H}_{\text{RAQR}}$ in RAQRs, we relate the physical passband quantities to their complex baseband equivalents. The received RF passband signal $x(t)$ with E-field amplitude U_x and power \mathcal{P}_x has a complex baseband representation $x_b(t) = \sqrt{\mathcal{P}_x}e^{j\theta_x}$. The E-field and power are related by $\mathcal{P}_x = U_x^2 A_e / (2Z_0)$ with a equivalent aperture A_e , and $Z_0 = 1/(c\epsilon_0)$ is the impedance of free space. The physical output passband IF voltage $\tilde{V}(t)$ is related to its complex baseband equivalent $\tilde{V}_b(t)$ by

$$\tilde{V}(t) = \Re(\sqrt{2}\tilde{V}_b(t)e^{j2\pi f_\delta t}). \quad (24)$$

We define $C_p = 2\sqrt{G_{\text{PD}}}\alpha\sqrt{\mathcal{P}_l\mathcal{P}_1(\Omega_{\text{LO}})\kappa_1\sin(\varphi_1)}$ and rewrite $\tilde{V}(t)$ in Eq. (21) to match the form of Eq. (24),

which can be expressed as

$$\tilde{V}(t) = C_p U_x \Re(e^{j(2\pi f_\delta t + \theta_\delta)}) = \Re(C_p U_x e^{j\theta_\delta} e^{j2\pi f_\delta t}). \quad (25)$$

By comparing this to Eq. (24), we can solve for $\tilde{V}_b(t)$:

$$\sqrt{2}\tilde{V}_b(t) = C_p U_x e^{j\theta_\delta} = C_p U_x e^{j(\theta_x - \theta_y)}. \quad (26)$$

Substituting $U_x = \sqrt{2Z_0/A_e}|x_b(t)|$ and $e^{j\theta_x} = x_b(t)/|x_b(t)|$, we have

$$\begin{aligned} \tilde{V}_b(t) &= \frac{1}{\sqrt{2}}C_p\sqrt{\frac{2Z_0}{A_e}}|x_b(t)|\frac{x_b(t)}{|x_b(t)|}e^{-j\theta_y} \\ &= \left[\frac{2\sqrt{G_{\text{PD}}}\alpha\sqrt{Z_0\mathcal{P}_l\mathcal{P}_1(\Omega_{\text{LO}})\kappa_1\sin(\varphi_1)}}{\sqrt{A_e}}e^{-j\theta_y}\right]x_b(t). \end{aligned} \quad (27)$$

The complete complex baseband transfer function of the RAQR is given by

$$\mathcal{H}_{\text{RAQR}} = \frac{2\alpha\sqrt{Z_0G_{\text{PD}}\mathcal{P}_l\mathcal{P}_1(\Omega_{\text{LO}})\kappa_1\sin(\varphi_1)}}{\sqrt{A_e}}e^{-j\theta_y}. \quad (28)$$

Let the transmitted baseband signal of RF transmitter be s_b and the wireless channel be h . The signal at the receiver aperture of RAQR is $x_b = \sqrt{A_e}hs_b$. Based on the detected voltage \tilde{V}_b , the end-to-end baseband signal model of RAQR can be expressed as

$$\tilde{V}_b = \sqrt{A_e}\mathcal{H}_{\text{RAQR}}hs_b + w \triangleq \sqrt{\beta}\Phi hs_b + w, \quad (29)$$

where $\beta = 4\alpha^2G_{\text{PD}}Z_0\mathcal{P}_l\mathcal{P}_1(\Omega_{\text{LO}})\kappa_1^2\sin^2(\varphi_1)$ denotes the effective power gain of the RAQR and $\Phi = \mathcal{H}_{\text{RAQR}}/|\mathcal{H}_{\text{RAQR}}| = \Phi = e^{-j\theta_y}$ denotes the phase response by locking the optical LO phase ϕ_l to maximize the signal amplitude, i.e., setting $\sin(\varphi_1) \approx 1$. In the RAQR, $w \sim \mathcal{CN}(0, \sigma_w^2(s_b))$ denotes the signal-related noise [26]. The noise power $\sigma_w^2(s_b) = N_{\text{QPN}} + N_{\text{PSN}} + N_{\text{ITN}}$ is the sum of quantum projection noise (QPN) N_{QPN} , photon shot noise (PSN) N_{PSN} , and intrinsic thermal noise (ITN) from electronics N_{ITN} .

In particular, the RAQR couples to the environmental electromagnetic vacuum, introducing the widely known black-body radiation (BBR) noise caused by the thermal field at environmental temperature T_{env} on Rydberg atom sensors. Since RAQRs operate as coherent quantum sensors, the incoherent thermal fields do not drive the coherent Rabi oscillations required for signal detection [35]. Instead, BBR induces random transitions between Rydberg states, leading to population redistribution and decoherence. The impact of BBR can be modeled as a thermal decoherence rate Γ_{BBR} that broadens the Rydberg states, which is given by [35], [36]

$$\Gamma_{\text{BBR}} \approx \frac{4\alpha_{\text{eff}}^3 k_B T_{\text{env}}}{3n_{\text{eff}}^2 \hbar}, \quad (30)$$

where k_B is a Boltzmann constant. α_{eff} is a fine-structure constant and n_{eff} is a effective principal quantum number.

Remark 1: In classical RF receivers, the BBR noise is also termed as thermal noise, where BBR manifests as the typical additive white Gaussian noise (AWGN), and hence the theoretical noise floor is fixed at -174 dBm/Hz due to thermal power density $k_B T_{\text{env}}$ [37]. However, the impact of BBR in RAQRs is not as an additive noise source, but as a thermal decoherence rate that broadens the Rydberg states, where the authors of [35] observed the sensitivity is only reduced by 0.1 % at $T_{\text{env}} = 773.15$ K based on

practical experiments. Indeed, treating BBR simply as an AWGN source would mathematically bound both atomic and electronic receivers to the same fundamental thermal noise floor, negating the quantum advantage of the RAQR.

For other dominated noise sources, the power spectral density of ITN with a system bandwidth B_{RAQR} is given by

$$N_{\text{ITN}} = k_B T_{\text{PD}} G_{\text{PD}} B_{\text{RAQR}}, \quad (31)$$

where T_{PD} is the equivalent noise temperature and B_{RAQR} denotes the communication bandwidth of RAQRs. In the BCOD scheme, the signal power scales with strong \mathcal{P}_l while N_{ITN} remains constant, resulting in the optical noise dominating thermal noise. Then, the PSN power is given by

$$N_{\text{PSN}} = 2qG_{\text{PD}}\alpha(\mathcal{P}_l + \mathcal{P}_1)B_{\text{RAQR}}, \quad (32)$$

where q is the elementary charge. Moreover, the QPN power can be expressed as

$$N_{\text{QPN}} = \frac{\beta}{2Z_0} \left(\frac{\hbar\sqrt{\Gamma_{\text{EIT}}}}{\mu_{45}\sqrt{N_m}} \right)^2 B_{\text{RAQR}}, \quad (33)$$

where $N_m = \pi r_0^2 d N_a$ denotes the number of Rydberg-state atoms within probe laser with beam radius r_0 .

Remark 2: While the superheterodyne RAQRs predominantly emphasizes the conventional optical mixing constraint $\Omega_{\text{sig}} \ll \Omega_{\text{LO}}$ to construct the linear response regime, the fundamental atomic saturation limit $\Omega_{\text{sig}} \ll \Gamma_{\text{EIT}}$ bounded by the EIT linewidth cannot be overlooked. In practical high-power scenarios, violating these conditions leads to two distinct nonlinearity limitations: 1) the atomic saturation effect when $\Omega_{\text{sig}} \approx \Gamma_{\text{EIT}}$, where strong fields depopulate the ground state and compress the susceptibility; and 2) the LO-signal mixing saturation when $\Omega_{\text{sig}} \approx \Omega_{\text{LO}}$, where the strong signal breaks the linear heterodyne assumption. Consequently, the dynamic range of RAQRs naturally dictates a dual-regime paradigm: the superheterodyne method is suitable for highly-sensitive weak-signal reception, whereas the ATS effect remains the mandatory mechanism for strong-field detection.

III. Performance Comparison: 2C4L-RAQR vs. 3C5L-RAQR

Building upon the established foundational models in Section II, this section presents a quantitative performance analysis and comparison between the conventional 2C4L-RAQR and the exhibited 3C5L-RAQR.

A. Scaling Laws of SNR

Consider a Rayleigh fading channel denoted by the complex coefficient $h \sim \mathcal{CN}(0,1)$ and leveraging the RAQR signal model derived in Eq. (29), we can establish an end-to-end relationship between the received baseband signal power P_S at the RAQR and the transmit power P_t at the RF transmitter, which is given by [38]

$$P_S = \beta |\Phi|^2 \frac{P_t G_t}{4\pi L^2} |h|^2 = P_t \frac{G_t \kappa_2 |h|^2}{4\pi L^2} |\chi'_{s,5L}|^2, \quad (34)$$

where G_t is the transmit antenna gain and L is the distance between the transmitter and the receiver. $\kappa_2 \triangleq$

$4G_{\text{PD}}\alpha^2 Z_0 \mathcal{P}_l \mathcal{P}_1 \left(\frac{\pi d \mu_{45}}{\lambda_p \hbar} \right)^2 \sin^2(\varphi_1)$ aggregates the optoelectronic conversion gain and optical path parameters.

Lemma 3: The analytical solution of atomic transconductance $\chi'_{s,5L}$ under weak-probe field approximation in the 3C5L-RAQR is given by

$$\chi'_{s,5L} = \left(\frac{K \Omega_{\text{LO}}}{2} \right) \left[\frac{-(i\Omega_p/2)(|\Omega_d|^2/4)(|\Omega_c|^2/4)}{f_2^2 f_3^2 f_4^2 f_5} \right], \quad (35)$$

where $K = \frac{N_a |\mu_{12}|^2}{\epsilon_0 \hbar \Omega_p}$ and the nested denominators are

$$f_5 = (i\Delta_5 - \Gamma_{51}), \quad (36)$$

$$f_4 = (i\Delta_4 - \Gamma_{41}) + |\Omega_{\text{RF}}|^2/(4f_5), \quad (37)$$

$$f_3 = (i\Delta_3 - \Gamma_{31}) + |\Omega_c|^2/(4f_4), \quad (38)$$

$$f_2 = (i\Delta_2 - \Gamma_{21}) + |\Omega_d|^2/(4f_3). \quad (39)$$

Proof: Please refer to Appendix C for more details. ■

The atomic transconductance $\chi'_{s,5L}$ is determined by the nested denominators $f_n, n \in \{2, \dots, 5\}$. Considering a thermal atom with velocity v , f_n can be rewritten as

$$f_n(v) = i(\Delta_n - \Delta_k v) - \Gamma_{n1}. \quad (40)$$

where Δ_k denotes the wavevector mismatch of lasers.

In the conventional 2C4L-RAQR, the large wavelength mismatch results in a significant residual wavevector Δk_{4L} . The denominators $f_3(v)$ and $f_4(v)$ are dominated by the Doppler shift term $i(\Delta_k v)$ with $\Delta_k = |k_p - k_c|$. Following Eq. (5), the effective EIT linewidth is dominated by $\Gamma_{\text{Res}}^{4L} = \frac{\Gamma_2}{|k_p|} \Delta k$, which is much larger than the original decay rates Γ_{n1} . Consequently, the atomic sensitivity of the 2C4L-RAQR is limited by this MHz-scale broadening rather than the natural linewidths. For the convenience of performance analysis by exhibiting the upper bound of the atomic transconductance χ'_s , suppose the resonant frequency and the weak-field power broadening effects [27], [39], i.e., $|\Omega|^2/|f_{n+1}| \ll \Gamma_{n1}$, we have

$$\chi'_{s,4L} \propto \frac{1}{|f_2^2 f_3^2 f_4|} \propto \frac{1}{\Gamma_{21}^2 (\Gamma_{31} + \Gamma_{\text{Res}}^{4L})^2 (\Gamma_{41} + \Gamma_{\text{Res}}^{4L})}, \quad (41)$$

where the term Γ_{Res}^{4L} dominates the denominator, significantly suppressing the atomic response.

The 3C5L-RAQR architecture utilizes a three-photon resonance condition, i.e., $\vec{k}_p + \vec{k}_d + \vec{k}_c \approx 0$, to cancel the Doppler effect, where the residual Doppler linewidth $\Gamma_{\text{Res}}^{5L} = \frac{\Gamma_2}{|k_p|} |k_p - k_d + k_c|$ is much smaller than the Γ_{Res}^{4L} . The terms f_n are dominated by the natural linewidths Γ_{n1} . The atomic sensitivity scales as

$$\chi'_{s,5L} \propto \frac{1}{|f_2^2 f_3^2 f_4^2 f_5|} \propto \frac{1}{\Gamma_{21}^2 \Gamma_{31}^2 (\Gamma_{41} + \Gamma_{\text{Res}}^{5L})^2 (\Gamma_{51} + \Gamma_{\text{Res}}^{5L})}. \quad (42)$$

Remark 3: Compared to 2C4L-RAQR, the 3C5L-RAQR introduces an additional linewidth term Γ_{31} in the denominator, originating from the extra intermediate transition excited by the dressing laser. The sensitivity scaling is determined by the product of the linewidths along the excitation path. However, the bottleneck in 2C4L-RAQR is the squared MHz-scale residual Doppler width Γ_{Res}^{4L} . Although the 3C5L-RAQR adds an extra term Γ_{31} , it replaces the MHz-scale term Γ_{Res}^{4L} with a squared kHz-scale term Γ_{Res}^{5L} , translating into a massive enhancement in macroscopic sensitivity.

In the RAQR, the sensitivity of RF field detection is inversely proportional to the EIT linewidth Γ_{EIT} , and hence the SNR evaluation of the RQAR is also related to Γ_{EIT} . The EIT linewidth Γ_{EIT} that accounts for nature decay rate [27], BBR-induced broadening [35], and other external broadening mechanisms [2], [25], [40], can be defined as

$$\Gamma_{\text{EIT}} = \Gamma_{\text{Res}} + \frac{\Gamma_{\text{Ryd}}^{\text{nat}} + \Gamma_{\text{BBR}}}{2} + \frac{\Omega_{\text{AT}}}{\Gamma_2} + \frac{v_{\text{th}}}{r_0} + \Gamma_{\text{d}}, \quad (43)$$

where $\Gamma_{\text{Ryd}}^{\text{nat}}$ denotes the natural decay rate of the sensing Rydberg state, i.e., $\Gamma_{\text{Ryd}}^{\text{nat}} = \Gamma_3^{4\text{L}}$ for 2C4L-RAQR and $\Gamma_{\text{Ryd}}^{\text{nat}} = \Gamma_4^{5\text{L}}$ for 3C5L-RAQR. The term $\Omega_{\text{AT}}/\Gamma_2$ describes the power broadening effect governed by the intermediate state decay Γ_2 , where $\Omega_{\text{AT}} = |\Omega_{\text{c}}|^2 + |\Omega_{\text{LO}}|^2$ denotes the effective power broadening of the EIT window is dictated by the ATS distance for superheterodyne RAQRs under the case of the weak probe laser. The term $\frac{v_{\text{th}}}{r_0}$ denotes transit-time broadening of thermal atoms, where $v_{\text{th}} = \sqrt{2k_{\text{B}}T_{\text{atom}}/m}$ denotes the most probable transverse velocity component and is orthogonal to v_z in Eq. (4). Here, m is atomic mass. The dephasing term Γ_{d} includes other external broadening effects, e.g., atom collision and laser linewidths [40]. For the residual Doppler broadening, the term $\Gamma_{\text{Res}}^{4\text{L}}$ is significant due to wavevector mismatch for 2C4L-RAQR, whereas in 3C5L-RAQR, $\Gamma_{\text{Res}}^{5\text{L}}$ is small owing to the Doppler-cancellation configuration. Hence, the EIT linewidth of the 2C4L-RAQR is dominated by $\Gamma_{\text{EIT}}^{4\text{L}} \approx \Gamma_{\text{Res}}^{4\text{L}} \gg \Gamma_{\text{EIT}}^{5\text{L}}$ [16].

The SNR $\gamma_{\text{RAQR}}^j, j \in \{4\text{L}, 5\text{L}\}$ for the RAQR is given by

$$\gamma_{\text{RAQR}}^j = \frac{P_{\text{S}}}{N_{\text{PSN}} + N_{\text{QPN}} + N_{\text{ITN}}}. \quad (44)$$

Key Takeaway 1: The SNR scaling law in the RAQR leads to two operating regimes:

- Photon Shot Limit (PSL) Regime: If N_{PSN} dominates typically at high LO power in Eq. (32), the SNR advantage of the 3C5L-RAQR comes from signal enhancement:

$$\frac{\gamma_{\text{RAQR}}^{5\text{L}}}{\gamma_{\text{RAQR}}^{4\text{L}}} \approx \frac{P_{\text{S}}^{5\text{L}}/N_{\text{PSN}}^{5\text{L}}}{P_{\text{S}}^{4\text{L}}/N_{\text{PSN}}^{4\text{L}}} \propto \frac{\mathcal{P}_0^{5\text{L}}}{\mathcal{P}_0^{4\text{L}}} \left| \frac{\chi'_{s,5\text{L}}}{\chi'_{s,4\text{L}}} \right|^2 \propto \frac{\mathcal{P}_0^{5\text{L}}}{\mathcal{P}_0^{4\text{L}}} \left(\frac{\Gamma_{\text{EIT}}^{4\text{L}}}{\Gamma_{\text{EIT}}^{5\text{L}}} \right)^4. \quad (45)$$

- Standard Quantum Limit (SQL) Regime: If the system is optimized to reach the atomic limit dominated by N_{QPN} , the SNR gains between 5L and 4L RAQRs become

$$\frac{\gamma_{\text{RAQR}}^{5\text{L}}}{\gamma_{\text{RAQR}}^{4\text{L}}} \approx \frac{P_{\text{S}}^{5\text{L}}/N_{\text{QPN}}^{5\text{L}}}{P_{\text{S}}^{4\text{L}}/N_{\text{QPN}}^{4\text{L}}} \propto \frac{\beta^{5\text{L}}/(\beta^{5\text{L}}\Gamma_{\text{EIT}}^{5\text{L}})}{\beta^{4\text{L}}/(\beta^{4\text{L}}\Gamma_{\text{EIT}}^{4\text{L}})} \propto \frac{\Gamma_{\text{EIT}}^{4\text{L}}}{\Gamma_{\text{EIT}}^{5\text{L}}}. \quad (46)$$

Fig. 5 decomposes the received SNR into two fundamental PSL and SQL regimes, where the 2C4L- and 3C5L-RAQRs are evaluated under different probe laser powers $\mathcal{P}_0^{4\text{L}}$. When operating under an identical probe laser power $\mathcal{P}_0^{4\text{L}} = 0.05$ mW, the 3C5L-RAQR architecture demonstrates a colossal sensitivity advantage, while the 2C4L-RAQR suffers from a catastrophic collapse in the PSL regime. This enormous PSN gap visually corroborates the fourth-power scaling penalty derived in Eq. (45). Due

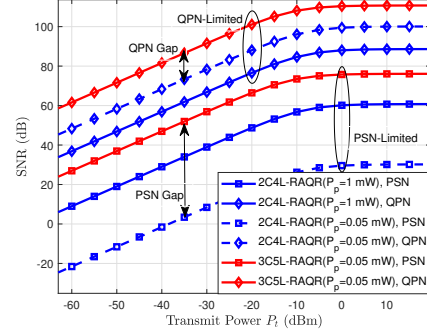


Fig. 5. SNR performance under different noise regimes of RAQRs.

to the severe residual Doppler mismatch in the 2C4L configuration, the macroscopic transconductance diminishes exponentially, leaving the weak signal entirely submerged by PSN. To mitigate this severe signal loss, a conventional workaround for the 2C4L-RAQR is to drastically increase the optical driving power, e.g., $\mathcal{P}_0^{4\text{L}} = 1$ mW. While this brute-force power injection artificially amplifies the transconductance to rescue the PSL, it induces severe power broadening to increase $\Gamma_{\text{EIT}}^{4\text{L}}$ and breaks the weak-probe approximation. As established in Eq. (46), the SQL is strictly bottlenecked by $1/\Gamma_{\text{EIT}}^{4\text{L}}$. Hence, the intense probe field fails to improve the SQL for the 2C4L-RAQR.

B. Communication Bandwidth and Capacity

For the RAQR, the communication bandwidth B_{RAQR} is bounded by the transient response speed of the system, i.e., the transient relaxation time τ_f required for the Rydberg atoms to establish a new steady state upon the signal variations [2]. In practical room-temperature vapor cells, this transient response is governed not only by the internal cascade decay of atomic states but also macroscopically constrained by the transit time of atoms flying across the laser beam profile and the power broadening of lasers or other signal fields. The baseband instantaneous bandwidth can be defined as [2], [41]

$$B_{\text{RAQR}}^j \approx \frac{1}{2\pi\tau_f^j}. \quad (47)$$

In Section IV-D, we will elaborate the exact numerical solution of B_{RAQR}^j from the time-dependent Lindblad master equation.

The ergodic channel capacity of RAQRs is expressed as⁴

$$C_{\text{RAQR}}^j = B_{\text{RAQR}}^j \mathbb{E}_{\mathbf{H}} \left[\log_2 \det \left(\mathbf{I} + \gamma_{\text{RAQR}}^j \mathbf{H}\mathbf{H}^H \right) \right]. \quad (48)$$

To evaluate the relative performance of different receiver architectures, we consider a classical RF receiver utilizing

⁴In fact, the signal-dependent noise in RAQRs is fundamentally coupled with the RF signal state, i.e., the \mathcal{P}_1 -related PSN in Eq. (32), Γ_{EIT} -related QPN in Eq. (33) as well as non-AWGN BBR noise. Hence, the classical Shannon channel capacity formula that requires standard AWGN distribution is no longer applicable for RAQRs [42]. In this work, considering the weak Ω_{sig} and the strong Ω_{LO} , we adopt the Gaussian achievable rate as a tractable performance metric and model the effective SNR γ_{RAQR}^j by incorporating the signal-dependent noise term.

a standard conductor antenna. The isotropic antenna captures power through its effective aperture $A_{\text{CL}} = G_r \frac{\lambda_{\text{RF}}^2}{4\pi}$, where G_r denotes the antenna gain. Given $\mathbb{E}[|h|^2] = 1$, the averaged received signal power $P_{S,\text{CL}}$ after the LNA is given by

$$P_{S,\text{CL}} = \frac{P_t G_t}{4\pi L^2} G_{\text{LNA}} A_{\text{CL}} = P_t \frac{G_t G_r G_{\text{LNA}} \lambda_{\text{RF}}^2}{(4\pi L)^2}. \quad (49)$$

where G_{LNA} denotes the gain of the LNA.

In this work, we refer to the noise power modeling in [26] in classical RF receiver, which is given by

$$P_{N,\text{CL}} = k_B T_{\text{env}} F G_{\text{LNA}} B_{\text{CL}}. \quad (50)$$

where F is the noise factor of the holistic system, and B_{CL} is the bandwidth of the classical RF receiver.

The SNR for the classical RF receiver is expressed as

$$\gamma_{\text{CL}} = \frac{P_{S,\text{CL}}}{P_{N,\text{CL}}} = \frac{G_t G_r \lambda_{\text{RF}}^2 P_t}{(4\pi L)^2 k_B T_{\text{env}} F B_{\text{CL}}}. \quad (51)$$

The ergodic channel capacity of the classical RF receiver is given by

$$C_{\text{CL}} = B_{\text{CL}} \mathbb{E}_{\mathbf{H}} [\log_2 \det(\mathbf{I} + \gamma_{\text{CL}} \mathbf{H} \mathbf{H}^H)]. \quad (52)$$

Note that for the classical RF receiver, the bandwidth B_{CL} is a designable parameter to determine the filter width, whereas for the RAQR, the bandwidth B_{RAQR}^j is physically constrained by the atomic parameters, laser intensity and RF signal field, which is generally far less than classical RF receiver.

C. Spectrum Access Range

In RAQR, the choice of excitation pathway dictates the accessible RF frequencies. The energy of a Rydberg state is $E_{n,l} = -R_y / (n - \delta_l)^2$, where R_y is a Rydberg constant and δ_l is the quantum defect that decreases rapidly with l [40], [43]. In 2C4L-RAQR, the atomic excitation path is $S \rightarrow P \rightarrow D$. In a transition like $|nD\rangle \rightarrow |(n+1)P\rangle$ has a frequency:

$$f_c \approx \frac{R_y}{2\pi\hbar} \left| \frac{1}{(n - \delta_D)^2} - \frac{1}{(n+1 - \delta_P)^2} \right|. \quad (53)$$

The large difference between δ_P and δ_D results in f_c in the high-frequency range. The large energy difference restricts 2C4L-RAQR to high-GHz or THz detection, and is physically incapable of resonant detection in the UHF/VHF bands.

Key Takeaway 2: The exhibited 3C5L-RAQR provides a flexible platform for accessing different frequency bands.

- **Microwave Access:** Following a similar atom transition path with 2C4L-RAQR to populate P-states, i.e., $S \rightarrow P \rightarrow S \rightarrow P$ in Section II-B, allowing for microwave-frequency access in GHz/THz range.
- **UHF/VHF Access:** The alternative schemes, e.g., $S \rightarrow P \rightarrow D \rightarrow F$, can be designed to populate high orbital angular momentum F-states. This unlocks access to high-quantum transitions, e.g., $|nF\rangle \rightarrow |nG\rangle$ [22], where the signal frequency is given by

$$f_c \approx \frac{R_y}{2\pi\hbar} \left| \frac{1}{(n - \delta_F)^2} - \frac{1}{(n - \delta_G)^2} \right|. \quad (54)$$

Since δ_F and δ_G are tiny [40], the energy difference is minimal. Using $1/(n-a)^2 - 1/(n-b)^2 \approx 2(a-b)/n^3$:

$$f_c \approx \frac{R_y |\delta_F - \delta_G|}{\pi\hbar n^3}. \quad (55)$$

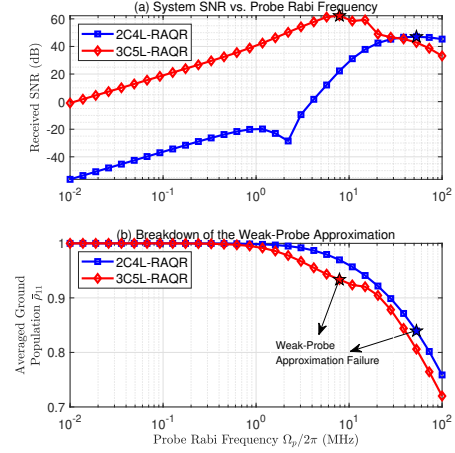


Fig. 6. Probe laser intensity vs. SNR and ground-state atom population.

We can observe that for transitions between high-angular-momentum states with similar quantum defects, the resonant frequency scales inversely with the principal quantum number n^{-3} and is proportional to the differential quantum defect $|\delta_F - \delta_G|$ [22]. In Fig. 7 of Section V, we show the exhibited 3C5L-RAQR is a unified platform for both microwave and UHF/VHF bands.

IV. Exact Numerical Modeling of Open Quantum Dynamics for Practical RAQRs

As established in Section II and III, the analytical models of steady-state atomic coherence ρ_{21} relies on the weak-probe approximation $\bar{\rho}_{11} \approx 1$. However, the conventional weak-probe approximation is fundamentally sub-optimal for maximizing sensitivity of RAQRs [28]. As shown in Fig. 6, the $\bar{\rho}_{11} \approx 1$ approximation will be broken in the optimal SNR peak of RAQRs, where the increase of probe laser intensity will cause the optical pumping of ground-state atoms. To rigorously evaluate the communication performance of RAQRs, in this section, we transition to a full computational physics framework, providing the exact numerical solution of the driven open quantum system.

A. Transit-Time Relaxation and Probability Conservation

In the exact numerical modeling, we recall the Lindblad master equation in Eq. (1) as

$$\frac{d\hat{\rho}}{dt} = -\frac{i}{\hbar} [\hat{H}, \hat{\rho}] + \mathcal{L}_{\text{decay}}(\hat{\rho}) + \mathcal{L}_{\text{transit}}(\hat{\rho}), \quad (56)$$

where $\mathcal{L}_{\text{decay}}$ denotes the intrinsic spontaneous emission and collision-induced dephasing. $\mathcal{L}_{\text{transit}}(\hat{\rho})$ denotes the transit-time relaxation, which describes thermal atoms traverse and exit the finite spatial cross-section of the driving laser beams [29], [40].

To obtain the exact steady-state coherence under $\frac{d\hat{\rho}}{dt} = 0$ without relying on the weak-probe approximation, we employ the Liouvillian superoperator formalism [44]. By mapping the $N \times N$ density matrix $\hat{\rho}$ onto a column vector

$|\rho\rangle\rangle$ of dimension $N^2 \times 1$ where $N = 5$ for the 3C5L-RAQR, the matrix differential equation is transformed into a linear algebraic system [44, Sec 4.1.2]:

$$\mathbf{L}|\rho\rangle\rangle = 0, \quad (57)$$

where \mathbf{L} is the 25×25 non-Hermitian Liouvillian matrix.

For a room-temperature vapor cell, the finite transit time of atoms crossing the localized laser beams constitutes a primary source of decoherence, where atoms exit the interaction region at a characteristic rate $\gamma_t = v_{\text{th}}/r_0$ [41], [45]. Critically, to maintain a constant atomic density within the sensing volume, the lost probability amplitude from exiting atoms must be precisely replenished by fresh and unpolarized atoms entering the beam in the ground state $|1\rangle$. We model the open-system boundary condition as [28]

$$\mathcal{L}_{\text{transit}}(\hat{\rho}) = -\gamma_t \hat{\rho} + \gamma_t \sum_{j=2}^N \rho_{jj} |1\rangle\langle 1|. \quad (58)$$

Since the system is trace-preserving, i.e., $\text{Tr}(\hat{\rho}) = 1$, the Liouvillian matrix \mathbf{L} is singular, possessing a zero eigenvalue. To circumvent this singularity and isolate the unique physical steady-state, we replace the final linearly dependent row of \mathbf{L} with the probability normalization constraint $\sum_{i=1}^N \rho_{ii} = 1$, yielding the modified Liouvillian matrix $\tilde{\mathbf{L}}$. This is a typical processing method in the direct numerical solvers [46], [47], which maps the homogeneous equation into a well-posed and invertible non-homogeneous linear system:

$$\tilde{\mathbf{L}}|\rho\rangle\rangle = \vec{b}, \quad (59)$$

where \vec{b} is a column vector containing 1 at the corresponding trace-condition index and 0 elsewhere.

B. Macroscopic Doppler Integration

The above steady-state vector $|\rho\rangle\rangle$ represents the response of a single atom at rest. However, the thermal vapor ensemble exhibits a Maxwell-Boltzmann velocity distribution as [25]

$$P(v) = \frac{1}{\sqrt{\pi}v_{\text{th}}} e^{-\frac{v^2}{v_{\text{th}}^2}}. \quad (60)$$

For an atom moving with velocity v along the optical axis, the Hamiltonian and the resulting Liouvillian superoperator become explicitly dependent on the atomic velocity v and the applied RF field Ω_{RF} . For any specific velocity class v , the exact microscopic steady-state density vector is computationally extracted by inverting the velocity-dependent non-homogeneous linear system:

$$|\rho(v, \Omega_{\text{RF}})\rangle\rangle = \tilde{\mathbf{L}}(v, \Omega_{\text{RF}})^{-1} \vec{b}. \quad (61)$$

The microscopic quantum coherence corresponding to the probe transition $\rho_{21}(v, \Omega_{\text{RF}})$ is then isolated by projecting the state vector onto the appropriate Liouville space basis element. The macroscopic atomic coherence $\bar{\rho}_{21}$ is formulated as the weighted integral over the thermal ensemble [16], [24], [25]:

$$\bar{\rho}_{21}(\Omega_{\text{RF}}) = \int_{-3v_{\text{th}}}^{3v_{\text{th}}} \rho_{21}(v, \Omega_{\text{RF}}) P(v) dv. \quad (62)$$

In the numerical implementation, this continuous integration is executed by discretizing the velocity domain

into N_v uniformly spaced velocity classes with a velocity resolution step of Δv :

$$\bar{\rho}_{21}(\Omega_{\text{RF}}) \approx \sum_{k=1}^{N_v} \rho_{21}(v_k, \Omega_{\text{RF}}) P(v_k) \Delta v. \quad (63)$$

C. Communication Baseband Bandwidth Extraction

While the steady-state transconductance determines the sensitivity of RAQRs, the maximum communication symbol rate is fundamentally bounded by the transient baseband bandwidth B_{RAQR} in Eq. (47). This dynamic limit is dictated by the system relaxation time τ_f , which describes how rapidly the macroscopic atomic coherence decays and establishes a new steady state when the incident RF signal is modulated. To computationally extract this bandwidth, we simulate the free induction decay of the atomic ensemble following an instantaneous RF turn-off [2]. For each velocity class v , the initial state is defined by the exact RF-driven steady state, $|\rho(v, t=0)\rangle\rangle = \tilde{\mathbf{L}}(v, \Omega_{\text{RF}})^{-1} \vec{b}$. When the RF field is turned off at $t > 0$, the transient evolution of the density vector is governed by the homogeneous differential equation:

$$\frac{d}{dt} |\rho(v, t)\rangle\rangle = \mathbf{L}_{\text{off}}(v) |\rho(v, t)\rangle\rangle, \quad (64)$$

where $\mathbf{L}_{\text{off}}(v)$ is the velocity-dependent Liouvillian superoperator evaluated at $\Omega_{\text{RF}} = 0$.

Rather than employing computationally expensive and unstable numerical integration methods, we obtain the exact continuous-time solution via eigendecomposition of the non-Hermitian Liouvillian matrix. Let $\mathbf{L}_{\text{off}}(v) = \mathbf{V}\mathbf{D}\mathbf{V}^{-1}$, where \mathbf{V} is the matrix of right eigenvectors and \mathbf{D} is the diagonal matrix of eigenvalues. The exact time-domain evolution for each velocity class is given by the matrix exponential [48]:

$$|\rho(v, t)\rangle\rangle = \mathbf{V} e^{\mathbf{D}t} \mathbf{V}^{-1} |\rho(v, 0)\rangle\rangle. \quad (65)$$

Due to the continuous superposition of velocity-dependent coherent states, the macroscopic free induction decay profile $\bar{\rho}_{21}(t)$ fundamentally deviates from a simple single-exponential function. Consequently, the macroscopic relaxation time τ_f cannot be expressed as a closed-form algebraic scalar. Instead, it can be defined as the $1/e$ decay threshold of the macroscopic transient response [2], where the e-folding timescale of the atomic dissipation maps the physical coherence loss to the -3 dB cutoff frequency of an equivalent baseband low-pass filter. Let $\bar{\rho}_{21}^{\text{on}}$ denote the initial driven steady-state coherence at $t = 0$ in the presence of the RF signal, and $\bar{\rho}_{21}^{\text{off}}$ denote the asymptotic background steady-state coherence driven solely by the optical fields after the RF signal is turned off. The exact relaxation time τ_f is computationally extracted by locating the root of the following implicit threshold-crossing equation:

$$\Im[\bar{\rho}_{21}(\tau_f)] = \Im[\bar{\rho}_{21}^{\text{off}}] + \frac{\Im[\bar{\rho}_{21}^{\text{on}}] - \Im[\bar{\rho}_{21}^{\text{off}}]}{e}. \quad (66)$$

Then, the baseband modulation bandwidth of the RAQR is obtained according to $B_{\text{RAQR}} = \frac{1}{2\pi\tau_f}$.

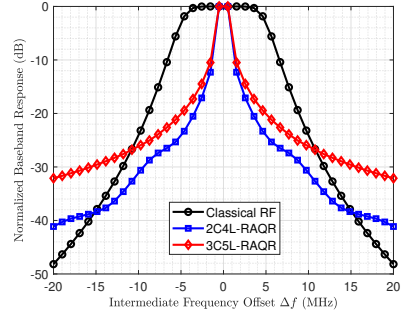
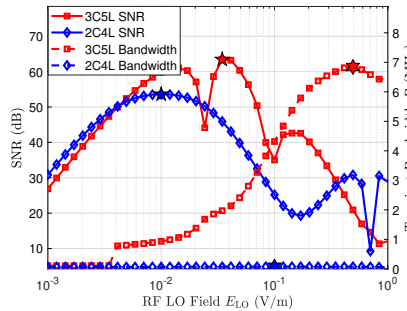
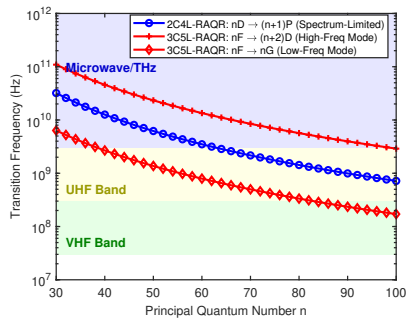


Fig. 7. Spectrum access range of RAQRs. Fig. 8. SNR-bandwidth tradeoff of RAQRs. Fig. 9. Frequency selectivity profiles of RAQRs.

TABLE I
Atomic Parameters for 2C4L- and 3C5L-RAQRs

Parameters	2C4L-RAQR	3C5L-RAQR
Vapor Cell Length d	10 cm	10 cm
Atom Density N_a	$1.5 \times 10^{11} \text{cm}^{-3}$	$1.5 \times 10^{11} \text{cm}^{-3}$
Probe Laser λ_p	852 nm	895 nm
Dressing Laser λ_d	N/A	636 nm
Coupling Laser λ_c	510 nm	2245 nm
Probe Beam Power \mathcal{P}_0	1 mW	50 μW
Coupling Beam Power \mathcal{P}_c	150 mW	40 mW
Dressing Beam Power \mathcal{P}_d	N/A	20 mW
Beam Radius r_0	0.38 mm	0.38 mm
RF LO Field U_y	0.03 V/m	0.03 V/m
Dipole Moment μ_{12}	$2.59 q_0 a_0$	$1.84 q_0 a_0$
Dipole Moment μ_{23}	$0.022 q_0 a_0$	$0.23 q_0 a_0$
Dipole Moment μ_{34}	$1443.48 q_0 a_0$	$0.019 q_0 a_0$
Dipole Moment μ_{45}	N/A	$1443.48 q_0 a_0$
Natural Decay Rates $\Gamma_2/2\pi$	5.22 MHz	4.56 MHz
Natural Decay Rates $\Gamma_3/2\pi$	2.73 kHz	0.98 MHz
Natural Decay Rates $\Gamma_4/2\pi$	0.57 kHz	0.57 kHz
Natural Decay Rates $\Gamma_5/2\pi$	N/A	2.73 kHz
Residual Dephasing Rates Γ_d	50 kHz	50 kHz

V. Numerical Results

Unless otherwise specified, we set $G_t = 10$ dB, $G_r = 5.5$ dB, $G_{\text{LNA}} = 60$ dB, and $F = 6$ for the classical RF receiver, while the photoelectric detection parameters of RAQRs are set to $G_{\text{PD}} = 30$ dB, $T_{\text{atom}} = T_{\text{PD}} = 290$ K, $\alpha = 0.8$ and $\mathcal{P}_l = 30$ mW [26]. Table I presents the specific atomic parameters for 2C4L- and 3C5L-RAQRs. The intrinsic properties of Rydberg atoms are computed by utilizing the open-source ARC library and publicly available measured data [40], [43], e.g., dipole moments μ_{ij} and natural decay rates Γ_n , while several controllable parameters of RAQRs are obtained by carrying out the parameter search based on the SNR metric, e.g., RF LO field U_y and laser powers. The distance L between the transmitter and the receivers is set to $L = 10$ m.

Fig. 7 presents the accessible RF frequencies against the principal quantum number n for different setups of RAQRs. While the 2C4L-RAQR can theoretically access the upper UHF band by employing very high principal quantum numbers, e.g., $n > 70$, it is physically constrained by the large energy gaps inherent in the $P \rightarrow D$ pathway. In contrast, the 3C5L-RAQR provides a more flexible access for UHF/VHF bands by utilizing high-angular-momentum transitions, which naturally reside in lower frequency ranges even at moderate n values. To fairly compare the performance between 2C4L- and 3C5L-

RAQRs, both RAQRs receive the impinging signal with the same carrier frequency f_c in this work. We consider a RF signal-induced atomic transition $|47D_{5/2}\rangle, |48P_{3/2}\rangle$, and hence $f_c = 6.94$ GHz according to Eq. (53).

Fig. 8 unveils the fundamental physical trade-off between the system sensitivity and the instantaneous bandwidth B_{RAQR} for RAQRs, modulated by the RF LO field U_y . Operating at a low U_y minimizes the power broadening effect, thereby preserving an ultra-sharp susceptibility peak χ'_s that maximizes the SNR. However, this sharp resonance dictates a long-lived coherent state, resulting in a sluggish transient relaxation time τ_f and a collapsed communication bandwidth. Conversely, increasing U_y accelerates the Rabi oscillations and forces rapid state evolution, which significantly expands the bandwidth but flattens the atomic dispersion curve, severely degrading the SNR. Therefore, it is difficult to achieve optimal bandwidth and SNR simultaneously using a common set of physical parameter settings. In the performance evaluation of this work, we adopt SNR-centric optimization to determine the physical parameters of the RAQR.

Fig. 9 compares the normalized baseband responses and frequency selectivity profiles of a classical RF receiver and RAQRs. Specifically, the baseband response for RAQRs is obtained by computing the magnitude of the atomic transconductance $|\chi'_s(\Delta f)|$, while the response for the classical RF receiver is modeled using a standard Butterworth filter with bandwidth $B_{\text{CL}} = 10$ MHz [49]. Although the classical RF receiver exhibits a broader and flatter response, the RAQRs demonstrate a significantly sharper selectivity profile. While this sharpness stems from a narrower instantaneous bandwidth, it serves as a distinct advantage: it intrinsically acts as a highly selective natural filter, offering superior out-of-band interference suppression compared to classical systems.

Fig. 10 compares the received SNR of different receivers, where the incident signal bandwidth is set to 100 kHz for a fair comparison. The 3C5L-RAQR significantly outperforms the 2C4L-RAQR, while the SNR performance between 2C4L-RAQR and classical RF receiver is close. The gain of 3C5L-RAQR is attributed to the suppression of residual Doppler broadening, which significantly enhances the atomic susceptibility χ'_s . As the incident signal power increases, the RAQRs exhibit a distinct saturation

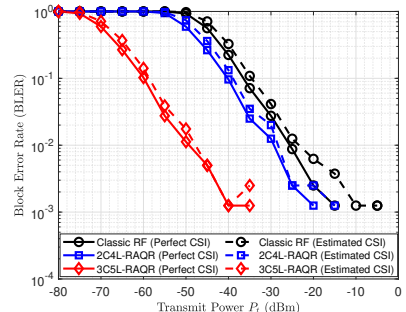
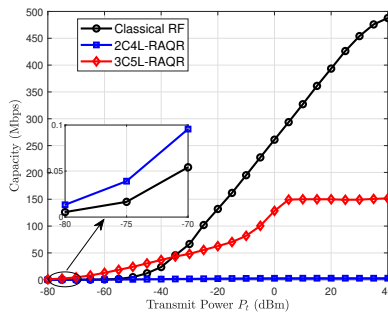
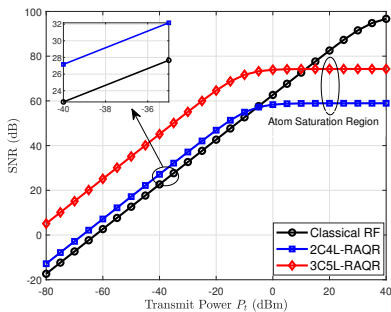


Fig. 10. Transmitting power P_t vs. SNR. Fig. 11. Transmitting power P_t vs. Capacity. Fig. 12. Transmitting power P_t vs. BLER.

effect due to the constraint of $\Omega_{\text{sig}} \ll \min\{\Gamma_{\text{EIT}}, \Omega_{\text{LO}}\}$.

Fig. 11 compares the achievable channel capacity of different receivers, where the feasible bandwidths B_{RAQR} of RAQRs are determined by Eq. (47) and the classical RF receiver bandwidth is set to $B_{\text{CL}} > B_{\text{RAQR}} = 10$ MHz. In the transmitted power-limited regime, i.e., low received SNR γ , approximating $\log(1 + \gamma) \approx \gamma$, the capacity scales as $C \approx B\gamma$. The high SNR advantages of RAQRs can provide a higher achievable channel capacity compared to the classic RF receiver. However, in the high transmitted power regime, approximating $\log(1 + \gamma) \approx \log(\gamma)$, the capacity scales as $C \approx B \log(\gamma)$. The linear reduction in bandwidth B dominates the logarithmic gain in SNR for RAQRs. Thus, for high-power and high-speed links, the classical RF receiver remains superior. In particular, the 3C5L-RAQR generally exhibits a higher baseline transient bandwidth compared to the 2C4L-RAQR, which is attributed to the spatial configuration of the laser beams. The Doppler-free configuration in the 3C5L-RAQR maximizes the effective optical pumping rate for all velocity classes, thereby eliminating the sluggish transient responses of off-resonant atoms that drag down the macroscopic bandwidth in the heavily inhomogeneously broadened 2C4L-RAQR.

Fig. 12 presents the BLER performance obtained via a link-level simulation, where the number of transmitted data blocks is 800 and each block consists of 256 symbols. The system employs 16-QAM modulation over a Rayleigh fading channel, utilizing a least square estimator for channel estimation and a linear minimum mean square error detector for signal recovery. We observe that the superior atomic sensitivity of the 3C5L-RAQR translates into a large BLER gain.

VI. Conclusion

In this paper, we investigated the 3C5L-RAQR architecture and exhibited an equivalent baseband signal model for high-sensitivity wireless communications, which effectively alleviates the residual Doppler broadening in thermal vapor cells. We provided the systemic performance analysis and the exact numerical solution method for RAQRs. Numerical analyses reveal that the 3C5L-RAQR achieves superior sensitivity, particularly in power-limited regimes and can serve as a versatile unified platform, capable

of accessing the strategic UHF/VHF spectrum via high-angular-momentum transitions. We also highlighted a no free lunch trade-off in RAQR design: the extreme sensitivity of the RAQR comes at the cost of a narrower instantaneous bandwidth and a lower saturation threshold. Future research will focus on enhancing the communication rate of the 3C5L-RAQR by integrating spatial or frequency-division multiplexing techniques.

Appendix A

Derivation of 3C5L Atomic Coherence ρ_{21}^{5L}

To obtain an analytical form of the steady-state coherence ρ_{21}^{5L} , we first determine the commutator $[\hat{H}_{5L}, \hat{\rho}]_{n1}$ based on the master equation $d\hat{\rho}/dt = 0$. For the 5×5 complex Hamiltonian matrix \hat{H}_{5L} defined in Eq. (6), the commutator is given by $[\hat{H}_{5L}, \hat{\rho}]_{ij} = \sum_{k=1}^5 H_{ik} \rho_{kj} - \rho_{ik} H_{kj}$. Thus, for the probe transition coherence $[\hat{H}_{5L}, \hat{\rho}]_{21}$, we formulate it as

$$[\hat{H}_{5L}, \hat{\rho}]_{21} = \frac{\hbar}{2} (\Omega_p^{5L})^* (\rho_{11} - \rho_{22}) - \hbar \Delta_2^{5L} \rho_{21} + \frac{\hbar}{2} \Omega_d^{5L} \rho_{31}. \quad (67)$$

According to the Lindblad master equation, the time evolution of ρ_{21} is given by

$$\dot{\rho}_{21} = -\frac{i}{2} (\Omega_p^{5L})^* (\rho_{11} - \rho_{22}) + i \Delta_2^{5L} \rho_{21} - \frac{i}{2} \Omega_d^{5L} \rho_{31} - \Gamma_{21} \rho_{21}. \quad (68)$$

Similarly, we obtain the evolution equations for the higher-order coherences ρ_{31} , ρ_{41} , and ρ_{51} . For notational conciseness, we omit the superscript 5L in the following derivation steps:

$$\dot{\rho}_{31} = -\frac{i}{2} \Omega_d^* \rho_{21} + i \Delta_3 \rho_{31} - \frac{i}{2} \Omega_c \rho_{41} + \frac{i}{2} \Omega_p^* \rho_{32} - \Gamma_{31} \rho_{31}, \quad (69)$$

$$\dot{\rho}_{41} = -\frac{i}{2} \Omega_c^* \rho_{31} + i \Delta_4 \rho_{41} - \frac{i}{2} \Omega_{\text{RF}} \rho_{51} + \frac{i}{2} \Omega_p^* \rho_{42} - \Gamma_{41} \rho_{41}, \quad (70)$$

$$\dot{\rho}_{51} = -\frac{i}{2} \Omega_{\text{RF}}^* \rho_{41} + i \Delta_5 \rho_{51} + \frac{i}{2} \Omega_p^* \rho_{52} - \Gamma_{51} \rho_{51}. \quad (71)$$

The steady-state condition enforces $\dot{\rho}_{21} = \dot{\rho}_{31} = \dot{\rho}_{41} = \dot{\rho}_{51} = 0$. By applying the weak-probe approximations ($\rho_{11} \approx 1$, $\rho_{ii \neq 1} \rightarrow 0$, and $\rho_{j2} \rightarrow 0$), the coupled system can be recast as

$$(i \Delta_2 - \Gamma_{21}) \rho_{21} - \frac{i}{2} \Omega_d \rho_{31} = \frac{i}{2} \Omega_p^*, \quad (72)$$

$$(i \Delta_3 - \Gamma_{31}) \rho_{31} - \frac{i}{2} \Omega_d^* \rho_{21} - \frac{i}{2} \Omega_c \rho_{41} = 0, \quad (73)$$

$$(i \Delta_4 - \Gamma_{41}) \rho_{41} - \frac{i}{2} \Omega_c^* \rho_{31} - \frac{i}{2} \Omega_{\text{RF}} \rho_{51} = 0, \quad (74)$$

$$(i\Delta_5 - \Gamma_{51})\rho_{51} - \frac{i}{2}\Omega_{\text{RF}}^*\rho_{41} = 0. \quad (75)$$

To isolate ρ_{21} , we iteratively back-substitute the higher-order coherences. From Eq. (75), we express ρ_{51} as

$$\rho_{51} = \frac{i\Omega_{\text{RF}}^*/2}{-(i\Delta_5 - \Gamma_{51})}\rho_{41}. \quad (76)$$

Substituting ρ_{51} into Eq. (74), we obtain:

$$\left[(i\Delta_4 - \Gamma_{41}) + \frac{|\Omega_{\text{RF}}|^2/4}{i\Delta_5 - \Gamma_{51}} \right] \rho_{41} = \frac{i}{2}\Omega_c^*\rho_{31}. \quad (77)$$

By defining the nested denominator $f_5 = i\Delta_5 - \Gamma_{51}$ and $f_4 = (i\Delta_4 - \Gamma_{41}) + |\Omega_{\text{RF}}|^2/(4f_5)$, we have $\rho_{41} = \frac{i\Omega_c^*/2}{f_4}\rho_{31}$. Following the same iterative procedure, we substitute ρ_{41} into Eq. (73) to obtain $\rho_{31} = \frac{i\Omega_c^*/2}{f_3}\rho_{21}$, where $f_3 = (i\Delta_3 - \Gamma_{31}) + |\Omega_c|^2/(4f_4)$. Finally, substituting ρ_{31} into Eq. (72) isolates ρ_{21} , yielding the continued-fraction solution in Eq.(7).

Appendix B

Derivation of the BCOD AC Voltage $\tilde{V}(t)$

The differential term P'_{mix} for Ω_{RF} in AC voltage $\tilde{V}(t)$ can be expressed as

$$P'_{\text{mix}} = \frac{d\sqrt{\mathcal{P}_1}}{d\Omega_{\text{RF}}} \cos(\phi_l - \phi_p) + \sqrt{\mathcal{P}_1} \frac{d\cos(\phi_l - \phi_p)}{d\Omega_{\text{RF}}}. \quad (78)$$

Using $\frac{d\sqrt{f}}{dx} = \frac{1}{2\sqrt{f}} \frac{df}{dx}$, we have

$$\frac{d\sqrt{\mathcal{P}_1}}{d\Omega_{\text{RF}}} = \frac{1}{2\sqrt{\mathcal{P}_1}} \left[\mathcal{P}_1 \left(-\frac{2\pi d}{\lambda_p} \Im(\chi'_s) \right) \right] = -\frac{\pi d\sqrt{\mathcal{P}_1}}{\lambda_p} \Im(\chi'_s), \quad (79)$$

$$\frac{d\cos(\phi_l - \phi_p)}{d\Omega_{\text{RF}}} = \sin(\phi_l - \phi_p) \frac{d\phi_p}{d\Omega_{\text{RF}}} = \sin(\phi_l - \phi_p) \frac{\pi d}{\lambda_p} \Re(\chi'_s). \quad (80)$$

Substituting these back into P'_{mix} at Ω_{LO} :

$$P'_{\text{mix}} = \frac{\pi d\sqrt{\mathcal{P}_1}}{\lambda_p} (\Re(\chi'_s) \sin(\phi_l - \phi_p) - \Im(\chi'_s) \cos(\phi_l - \phi_p)). \quad (81)$$

Using $\sin(A - B) = \sin A \cos B - \cos A \sin B$ and $\chi'_s = |\chi'_s|e^{i\psi_p}$, we have

$$P'_{\text{mix}} = \frac{\pi d\sqrt{\mathcal{P}_1}}{\lambda_p} |\chi'_s| (\cos(\psi_p) \sin(\phi_l - \phi_p) - \sin(\psi_p) \cos(\phi_l - \phi_p)) = \frac{\pi d\sqrt{\mathcal{P}_1}}{\lambda_p} |\chi'_s| \sin(\phi_l - \phi_p - \psi_p). \quad (82)$$

Letting $\varphi_1 = \phi_l - \phi_p - \psi_p$, we have

$$P'_{\text{mix}}(\Omega_{\text{LO}}) = \frac{\pi d\sqrt{\mathcal{P}_1}}{\lambda_p} |\chi'_s| \sin(\varphi_1). \quad (83)$$

Substituting this into $\tilde{V}(t) = 2\alpha\sqrt{G_{\text{PD}}}\mathcal{P}_i\Omega_{\text{sig}}(t)P'_{\text{mix}}(\Omega_{\text{LO}})$, we arrive at Eq. (21).

Appendix C

Derivation of Atomic Transconductance χ'_s

We decompose the derivative $\chi'_s = \left. \frac{\partial \chi}{\partial \Omega_{\text{RF}}} \right|_{\Omega_{\text{LO}}}$ into three parts. First, we define the RF coupling term from the continued fractions in Appendix A as $C_{\text{RF}} = |\Omega_{\text{RF}}|^2/4$. The chain rule is given by

$$\chi'_s = \frac{\partial \chi}{\partial \rho_{21}} \cdot \frac{\partial \rho_{21}^{5L}}{\partial C_{\text{RF}}} \cdot \frac{\partial C_{\text{RF}}}{\partial \Omega_{\text{RF}}}. \quad (84)$$

We evaluate each term:

1) $\partial \chi / \partial \rho_{21}^{5L}$: From Eq. (3), this is a constant K :

$$\frac{\partial \chi}{\partial \rho_{21}^{5L}} = K = \frac{N_a |\mu_{12}|^2}{\epsilon_0 \hbar \Omega_p}. \quad (85)$$

2) $\partial C_{\text{RF}} / \partial \Omega_{\text{RF}}$: Assuming a real-valued Ω_{LO} bias:

$$\frac{\partial C_{\text{RF}}}{\partial \Omega_{\text{RF}}} = \frac{\partial}{\partial \Omega_{\text{RF}}} \left(\frac{\Omega_{\text{RF}}^2}{4} \right) = \frac{\Omega_{\text{RF}}}{2}. \quad (86)$$

Evaluated at the LO bias, this gives $\frac{\Omega_{\text{LO}}}{2}$.

3) $\partial \rho_{21}^{5L} / \partial C_{\text{RF}}$: We define the nested denominators in Eq. (7) evaluated at Ω_{LO} as

$$f_5 = i\Delta_5 - \Gamma_{51}, \quad (87)$$

$$f_4 = (i\Delta_4 - \Gamma_{41}) + |\Omega_{\text{RF}}|^2/(4f_5), \quad (88)$$

$$f_3 = (i\Delta_3 - \Gamma_{31}) + |\Omega_c|^2/(4f_4), \quad (89)$$

$$f_2 = (i\Delta_2 - \Gamma_{21}) + |\Omega_d|^2/(4f_3). \quad (90)$$

We apply the chain rule $\frac{\partial \rho_{21}^{5L}}{\partial C_{\text{RF}}} = \frac{\partial \rho_{21}^{5L}}{\partial f_2} \cdot \frac{\partial f_2}{\partial f_3} \cdot \frac{\partial f_3}{\partial f_4} \cdot \frac{\partial f_4}{\partial C_{\text{RF}}}$:

$$\frac{\partial \rho_{21}^{5L}}{\partial C_{\text{RF}}} = \frac{-i\Omega_p/2 - |\Omega_d|^2/4 - |\Omega_c|^2/4}{f_2^2} \frac{1}{f_3^2} \frac{1}{f_4^2} \frac{1}{f_5}. \quad (91)$$

Hence, the full 3C5L atomic transconductance is given by

$$\chi'_{s, 5L} = \frac{K\Omega_{\text{LO}}}{2} \left[\frac{-(i\Omega_p/2)(|\Omega_d|^2/4)(|\Omega_c|^2/4)}{f_2^2 f_3^2 f_4^2 f_5} \right]. \quad (92)$$

The 2C4L derivation is a subset of the above, where $f_2 = (i\Delta_2 - \Gamma_{21}) + |\Omega_c|^2/(4f_3)$ and $f_3 = (i\Delta_3 - \Gamma_{31}) + C_{\text{RF}}/f_4$. The chain rule is shorter, which is given by

$$\frac{\partial \rho_{21}^{4L}}{\partial C_{\text{RF}}} = \frac{\partial \rho_{21}^{4L}}{\partial f_2} \cdot \frac{\partial f_2}{\partial f_3} \cdot \frac{\partial f_3}{\partial C_{\text{RF}}} = \frac{-i\Omega_p/2 - |\Omega_c|^2/4}{f_2^2} \frac{1}{f_3^2} \frac{1}{f_4}. \quad (93)$$

The full 2C4L atomic transconductance is given by

$$\chi'_{s, 4L} = \frac{K\Omega_{\text{LO}}}{2} \frac{(i\Omega_p/2)(|\Omega_c|^2/4)}{f_2^2 f_3^2 f_4}. \quad (94)$$

References

- [1] M. Saffman, T. G. Walker, and K. Mølmer, "Quantum information with Rydberg atoms," *Rev. Mod. Phys.*, vol. 82, no. 3, pp. 2313–2363, Aug. 2010.
- [2] D. H. Meyer, K. C. Cox, F. K. Fatemi, and P. D. Kunz, "Digital communication with Rydberg atoms and amplitude-modulated microwave fields," *Appl. Phys. Lett.*, vol. 112, no. 21, May 2018.
- [3] D. A. Anderson, R. E. Sapiro, and G. Raithel, "An atomic receiver for AM and FM radio communication," *IEEE Trans. Antennas Propag.*, vol. 69, no. 5, pp. 2455–2462, May 2021.
- [4] D. H. Wolpert and W. G. Macready, "No free lunch theorems for optimization," *IEEE Trans. Evol. Comput.*, vol. 1, no. 1, pp. 67–82, Apr. 1997.
- [5] D. Somaweera et al., "Rydberg atom-based sensors: Principles, recent advances, and applications," *Photonics*, vol. 12, no. 12, Dec. 2025.
- [6] J. A. Sedlacek, A. Schwettmann, H. Kübler, R. Löw, T. Pfau, and J. P. Shaffer, "Microwave electrometry with Rydberg atoms in a vapour cell using bright atomic resonances," *Nature Phys.*, vol. 8, no. 11, pp. 819–824, Nov. 2012.
- [7] C. L. Holloway, M. T. Simons, J. A. Gordon, and D. Novotny, "Detecting and receiving phase-modulated signals with a Rydberg atom-based receiver," *IEEE Antennas Wirel. Propag. Lett.*, vol. 18, no. 9, pp. 1853–1857, Sep. 2019.
- [8] D. H. Meyer, J. C. Hill, P. D. Kunz, and K. C. Cox, "Simultaneous multiband demodulation using a Rydberg atomic sensor," *Phys. Rev. Appl.*, vol. 19, no. 1, p. 014025, Jan. 2023.
- [9] M. Cui, Q. Zeng, and K. Huang, "Towards atomic MIMO receivers," *IEEE J. Sel. Areas Commun.*, vol. 43, no. 3, pp. 659–673, Mar. 2025.
- [10] T. Gong, C. Yuen, C. M. S. See, M. Debbah, and L. Hanzo, "Rydberg atomic quantum receivers for the multi-user MIMO uplink," in *Proc. IEEE Int. Conf. Commun. (ICC)*, 2025, pp. 4786–4791.

- [11] T. Gong, A. Chandra, C. Yuen, Y. L. Guan, R. Dumke, C. M. S. See, M. Debbah, and L. Hanzo, "Rydberg atomic quantum receivers for classical wireless communication and sensing," *IEEE Wireless Commun.*, vol. 32, no. 5, pp. 90–100, Oct. 2025.
- [12] T. Gong, C. Yuen, C. M. S. See, M. Debbah, and L. Hanzo, "Rydberg atomic quantum receivers for multi-target DOA estimation," *IEEE Trans. Veh. Technol.*, 2025.
- [13] M. Cui, Q. Zeng, M. Chen, Z. Wang, T. Mao, D. Zheng, and K. Huang, "Rydberg atomic receivers for multi-band communications and sensing," *IEEE Trans. Wireless Commun.*, vol. 25, pp. 13 384–13 400, Mar. 2026.
- [14] N. Thaicharoen, K. R. Moore, D. A. Anderson, R. C. Powell, E. Peterson, and G. Raithel, "Electromagnetically induced transparency, absorption, and microwave-field sensing in a Rb vapor cell with a three-color all-infrared laser system," *Phys. Rev. A*, vol. 100, p. 063427, Dec. 2019.
- [15] X. Zuo, Q. Li, D. Li, H. Wu, J. Sheng, and H. Wu, "High-power injection-locked blue laser for Rydberg atom-based sensing," *Opt. Express*, vol. 33, no. 14, pp. 29 247–29 254, Jul. 2025.
- [16] N. Prajapati, N. Bhusal, A. P. Rotunno et al., "Sensitivity comparison of two-photon vs three-photon Rydberg electrometry," *J. Appl. Phys.*, vol. 134, p. 023101, Jul. 2023.
- [17] N. Prajapati et al., "High angular momentum coupling for enhanced Rydberg-atom sensing in the very-high frequency band," *J. Appl. Phys.*, vol. 135, no. 7, Feb. 2024.
- [18] D. Song et al., "Continuous broadband Rydberg receiver using AC Stark shifts and Floquet states," *Appl. Phys. Lett.*, vol. 125, no. 19, Nov. 2024.
- [19] J. Hu et al., "Continuously tunable radio frequency electrometry with Rydberg atoms," *Appl. Phys. Lett.*, vol. 121, no. 1, Jul. 2022.
- [20] M. T. Simons et al., "Continuous radio-frequency electric-field detection through adjacent Rydberg resonance tuning," *Phys. Rev. A*, vol. 104, no. 3, p. 032824, Sep. 2021.
- [21] K. Ouyang, Y. Shi, M. Lei, and M. Shi, "Continuous broadband microwave electric field measurement in Rydberg atoms based on the DC Stark effect," *Appl. Phys. Lett.*, vol. 123, no. 26, Dec. 2023.
- [22] R. C. Brown, B. Kayim, M. A. Viray, A. R. Perry, B. C. Sawyer, and R. Wyllie, "Very-high-and ultrahigh-frequency electric-field detection using high angular momentum Rydberg states," *Phys. Rev. A*, vol. 107, no. 5, p. 052605, May 2023.
- [23] D. A. Anderson, R. E. Sapiro, and G. Raithel, "Rydberg atoms for radio-frequency communications and sensing: Atomic receivers for pulsed RF field and phase detection," *IEEE Aerosp. Electron. Syst. Mag.*, vol. 35, no. 4, pp. 48–56, Apr. 2020.
- [24] P. R. Berman and V. S. Malinovsky, *Principles of Laser Spectroscopy and Quantum Optics*. Princeton Univ. Press, 2011.
- [25] C. L. Holloway et al., "Electric field metrology for SI traceability: Systematic measurement uncertainties in electromagnetically induced transparency in atomic vapor," *J. Appl. Phys.*, vol. 121, no. 23, Jun. 2017.
- [26] T. Gong, J. Sun, C. Yuen, G. Hu, Y. Zhao, Y. L. Guan, C. M. S. See, M. Debbah, and L. Hanzo, "Rydberg atomic quantum receivers for classical wireless communications and sensing: Their models and performance," *arXiv preprint arXiv:2412.05554*, 2025.
- [27] J. Gea-Banacloche, Y. Li, S. Jin, and M. Xiao, "Electromagnetically induced transparency in ladder-type inhomogeneously broadened media: Theory and experiment," *Phys. Rev. A*, vol. 51, pp. 576–584, Jan. 1995.
- [28] D. H. Meyer, C. O'Brien, D. P. Fahey, K. C. Cox, and P. D. Kunz, "Optimal atomic quantum sensing using electromagnetically-induced-transparency readout," *Phys. Rev. A*, vol. 104, no. 4, p. 043103, Dec. 2021.
- [29] A. K. Mohapatra, T. R. Jackson, and C. S. Adams, "Coherent optical detection of highly excited Rydberg states using electromagnetically induced transparency," *Phys. Rev. Lett.*, vol. 98, no. 11, p. 113003, Mar. 2007.
- [30] J. Glick, B. E. Anderson, T. N. Nunley, J. Bingaman, J. J. Liu, D. H. Meyer, and P. Kunz, "Doppler-free rydberg spectroscopy in a warm vapor," *Physical Review A*, vol. 112, no. 6, p. 063726, Dec. 2025.
- [31] S. Mondal, D. Das, P. Dey, D. Bhattacharyya, and A. Bandyopadhyay, "Electromagnetically induced transparency, narrow absorption and transient response in a three-photon excitation process," *Optik*, vol. 265, p. 169410, Aug. 2022.
- [32] M. Jing, Y. Hu, J. Ma, H. Zhang, L. Zhang, L. Xiao, and S. Jia, "Atomic superheterodyne receiver based on microwave-dressed Rydberg spectroscopy," *Nat. Phys.*, vol. 16, pp. 911–915, Sep. 2020.
- [33] C. L. Holloway et al., "Broadband Rydberg atom-based electric-field probe for SI-traceable, self-calibrated measurements," *IEEE Trans. Antennas Propag.*, vol. 62, no. 12, pp. 6169–6182, Dec. 2014.
- [34] X.-H. Liu et al., "Continuous-frequency microwave heterodyne detection in an atomic vapor cell," *Phys. Rev. Appl.*, vol. 18, no. 5, p. 054003, Nov. 2022.
- [35] C. Kaur, P. Shen, D. Booth, A. Todd, and J. P. Shaffer, "The impact of thermal fields on Rydberg atom radio frequency sensors," *arXiv preprint arXiv:2508.17506*, 2025.
- [36] W. E. Cooke and T. F. Gallagher, "Effects of blackbody radiation on highly excited atoms," *Phys. Rev. A*, vol. 21, no. 2, p. 588, Feb. 1980.
- [37] L. W. Bussey, F. A. Burton, K. Bongs, J. Goldwin, and T. Whitley, "Quantum shot noise limit in a Rydberg RF receiver compared to thermal noise limit in a conventional receiver," *IEEE Sensors Lett.*, vol. 6, no. 9, pp. 1–4, Sep. 2022.
- [38] C. A. Balanis, *Antenna Theory: Analysis and Design*, 4th ed. Hoboken, NJ, USA: John Wiley & Sons, 2016.
- [39] N. Prajapati, N. Bhusal, A. P. Rotunno et al., "Sensitivity comparison of two-photon vs three-photon Rydberg electrometry," *J. Appl. Phys.*, vol. 134, no. 2, Jul. 2023.
- [40] N. Šibalić, J. D. Pritchard, C. S. Adams, and K. J. Weatherill, "ARC: An open-source library for calculating properties of alkali Rydberg atoms," *Comput. Phys. Commun.*, vol. 220, pp. 319–331, Nov. 2017.
- [41] J. Hu, Y. Jiao, Y. He, H. Zhang, L. Zhang, J. Zhao, and S. Jia, "Improvement of response bandwidth and sensitivity of rydberg receiver using multi-channel excitations," *EPJ Quantum Technol.*, vol. 10, no. 1, p. 51, Nov. 2023.
- [42] H. Ghourchian, G. Aminian, A. Gohari, M. Mirmohseni, and M. Nasiri-Kenari, "On the capacity of a class of signal-dependent noise channels," *IEEE Trans. Inf. Theory*, vol. 64, no. 12, pp. 7828–7846, Dec. 2018.
- [43] D. A. Steck, "Cesium D line data," <http://steck.us/alkalidata>, 2025.
- [44] —, "Quantum and atom optics," <http://steck.us/atomoptics>, 2007.
- [45] J. Sagle, R. K. Namiotka, and J. Huennekens, "Measurement and modelling of intensity dependent absorption and transit relaxation on the cesium D1 line," *J. Phys. B, At. Mol. Opt. Phys.*, vol. 29, no. 12, pp. 2629–2643, Jun. 1996.
- [46] S. M. Tan, "A computational toolbox for quantum and atomic optics," *J. Opt. B: Quantum Semiclass. Opt.*, vol. 1, no. 4, pp. 424–432, Aug. 1999.
- [47] J. R. Johansson, P. D. Nation, and F. Nori, "QuTiP 2: A Python framework for the dynamics of open quantum systems," *Comput. Phys. Commun.*, vol. 184, no. 4, pp. 1234–1240, Apr. 2013.
- [48] C. Moler and C. Van Loan, "Nineteen dubious ways to compute the exponential of a matrix, twenty-five years later," *SIAM Rev.*, vol. 45, no. 1, pp. 3–49, Jan. 2003.
- [49] H. Pfister, "Discrete-time signal processing," *Lecture Note*, [pfister.ee.duke.edu/courses/ece485/dtsp.pdf](http://ee.duke.edu/courses/ece485/dtsp.pdf), 2017.